Department of Physics and Astronomy
Heidelberg University

Bachelor Thesis in Physics
submitted by

Linus Alexander Kürpick

born in Speyer (Germany)

2024

Development of a 20-Channel Wavelength Division Multiplexer on a Si_3N_4 platform

This Bachelor Thesis has been carried out by Linus Alexander Kürpick at
the
Kirchhoff-Institut für Physik in Heidelberg
under the supervision of
Prof. Dr. Wolfram H. P. Pernice

Abstract

Transmitting photons over long distances poses a significant challenge due to attenuation. One effective strategy to address the rate-distance trade-off is to utilize wavelength division multiplexing (WDM), which combines light from multiple channels. Integrated photonics facilitates the simultaneous use of many channels, thereby enabling exceptionally high data rates. In this thesis the development progress of a multiplexer on a silicon nitride platform is presented, designed to combine light from 20 lasers with wavelengths ranging from 1550 nm to 1569 nm, at a spacing of 1 nm, and later to be used in a quantum key distribution (QKD) system. While simpler multiplexing methods, such as cascading structures, are available, they suffer from increased losses with higher channel counts and lack scalability. Therefore, add-drop ring resonators are selected as the primary multiplexing structure due to their better scalability and efficiency. Add-drop ring resonators efficiently transmit light of a specific wavelength and are complemented with bragg filters to achieve a large bandwith. Ring resonators with a Free spectral range (FSR) of (5.13 ± 0.12) nm an extinction ratio of 20 dB, and a transmission of 53% were realized, as well as Bragg filters with a central wavelength accuracy of (0.5 ± 0.4) nm and a bandwidth of 4.12 nm.

Zusammenfassung

Die Übertragung von Photonen über große Entfernungen stellt aufgrund der Übertragungsverluste eine große Herausforderung dar. Eine wirksame Strategie zur Bewältigung des Kompromisses zwischen der Übertragungsrate und der Entfernung ist das Wellenlängenmultiplexing (WDM), bei dem Licht aus mehreren Kanälen kombiniert wird. Integrierte Photonik erleichtert die gleichzeitige Nutzung vieler Kanäle in einer Faser und ermöglicht so außergewöhnlich hohe Datenraten. In dieser Arbeit wird der Entwicklungsfortschritt eines Multiplexers auf einer Siliziumnitrid Plattform vorgestellt, der das Licht von 20 Lasern mit Wellenlängen von 1550 nm bis 1569 nm und einer Schrittweite von 1 nm kombinieren soll, um später in einem Quantenschlüsselaustauschsystem (QKD) eingesetzt zu werden. Zwar gibt es einfachere Multiplexing-Methoden, wie z.B. Kaskadenstrukturen, doch leiden diese unter zunehmenden Verlusten bei höherer Kanalanzahl und mangelnder Skalierbarkeit. Daher werden Add-Drop-Ringresonatoren aufgrund ihrer besseren Skalierbarkeit und Effizienz als primäre Multiplexingstruktur ausgewählt. Add-Drop-Ringresonatoren übertragen effizient Licht einer bestimmten Wellenlänge und werden mit Bragg-Filtern ergänzt, um eine große Bandbreite zu erreichen. Es wurden Ringresonatoren mit einem freien Spektralbereich von $(5,13 \pm 0,12)$ nm, einem Extinktionsverhältnis von 20 dB und einer Transmission von 53% sowie Bragg-Filter mit einer Genauigkeit der zentralen Wellenlängen von $(0,5 \pm 0,4)$ nm und einer Bandbreite von $4,12$ nm realisiert.

Contents

1 Introduction

Due to the constant increase in the computing power of conventional computers and, in particular, the development of quantum computers, currently widespread encryption systems will in the foreseeable future no longer be secure [1]. As a result, new methods must be developed to address this problem. Mainly two approaches are being considered: The first one involves developing new cryptographic algorithms, known as post-quantum cryptography. These are very complex and yet fundamentally not secure against being decrypted by computers with sufficient computing power [2]. Another promising method is quantum cryptography, which uses quantum mechanical effects to encrypt data. Within quantum cryptography, one technique is quantum key distribution (QKD), in which a key known only to the sender and receiver is exchanged. In contrast to computationally secure protocols, which depend on unattainable amounts of resources to break the code, QKD systems offer intrinsic information technological security. Thus, QKD systems ensure that, with flawless implementation, they cannot be decrypted even by future, more powerful quantum computers [3].
To achieve high secret key rates in a QKD system, wavelength division multiplexing (WDM) can be utilized to enhance transmission speed. The goal of this project is to create a quantum encryption system with a record-high transmission rate. The transmission of photons over long distances is the main challenge, as they are attenuated while they are being transmitted and only relatively low data rates can be achieved even over short distances. One approach to overcoming the rate-distance trade-off in QKD systems is to bundle light from different channels, thereby enabling a very high data rate [4]. With a WDM system, precisely this is achieved, as light from different lasers is combined and transferred through a common waveguide using a device known as a multiplexer. The WDM system developed in this work is implemented as an photonic integrated circuit (PIC), because it simplifies the system by consolidating all optical functions into a single, compact device. A silicon nitride platform is used for the chip due to its low losses [5]. Managing twenty free-space channels, presents significant challenges and inefficiencies, which are mitigated by using an integrated photonic circuit. The aim of this bachelor's thesis is to desgin and determine all the necessary parameters for the multiplexer [4].

2 Theory

In the following chapter, the theory of the photonic chip and all its individual components is described. First, the concept of wavelength-division multiplexing (WDM) is introduced, as this is the key function of the chip. Wavelength-division multiplexing refers to a system in which light from multiple channels differentiable by wavelengths, is brought onto a common optical carrier [4]. This has the advantage of enabling very high data rates on individual optical fibers, as information from several channels can be transmitted in parallel. There are various approaches to implementing this technically, utilizing several integated photonic components, as well as techniques using bulk und fiber optics. To understand the multiplexer chip, we need to introduce four main components of integrated photonics. The simplest structures are waveguides, which are used to guide light on a photonic chip. Additionally, directional couplers are employed to transfer light between two waveguides. The two essential components for filtering light are ring resonators and Bragg filters. The theory behind these components is explained in the following.

2.1 Waveguide

The most fundamental component of integrated photonic circuits are waveguides. Generally, the function of waveguides is to transport light between two points with minimal loss. Thus, waveguides are analogous to optical fibers, which are commonly used in telecommunication. The basic structure of a waveguide consists of a higher refractive index material surrounded by a lower refractive index material [6]. There are various types of waveguides, but the physical principles are the same. To physically describe waveguides, one can use an approach based on ray optics or a description using Maxwell's equations. In figure 1, the previously described basic structure of a waveguide is illustrated using a cross-sectional view [6].

2.1.1 Ray Optics Picture

Since the ray optics approach is the more intuitive method for the physical description of light guidance within the waveguides, it will be discussed first. To describe the ray optics approach, we consider a core material (f) that is situated between a substrate (s) below and a cladding (c) above the core material. The regarded structure is depicted in figure 2. This arrangement is commonly referred to as a slab waveguide where the arrangement in the y and z directions is extended infinitely. For the analysis in the ray optics picture each material is characterized by its refractive index n_i. Depending

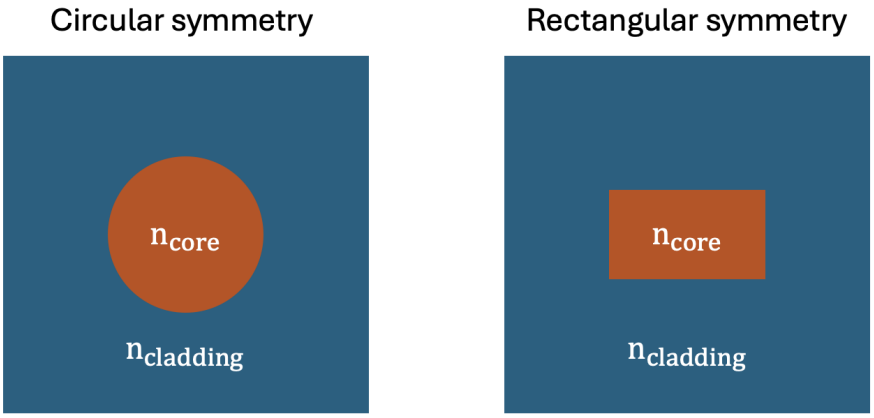

Figure 1: Cross sections of fundamental waveguide shapes. The propagation direction of the light is out of- or into the plane. n_{core} and n_{cladding} are the refractive indices of the core and cladding, respectively. The circular symmetry is utilized in optical fibers, figure adapted from [6], chap. 3, p. 32.

on the configuration of the refractive indices of the materials n_{i} and the incident angle θ, there are several possible outcomes. Therefore a beam in the core material is initially considered. Total internal reflection (TIR) is said to occur when this beam is completely reflected at the interface between the core material and the cladding material as well as at the interface between the core and the substrate material. Each time the beam reaches the interface, it comes from within the core material. This case is desirable when constructing waveguides, as it ensures that the light is guided inside the waveguide [6].
To mathematically describe TIR, we will first define the two critical angles,

$$\theta_{\text{c}} \equiv \arcsin\left(\frac{n_{\text{c}}}{n_{\text{f}}}\right) \tag{2.1}$$

$$\theta_{\text{s}} \equiv \arcsin\left(\frac{n_{\text{s}}}{n_{\text{f}}}\right) \tag{2.2}$$

that can be used to determine whether a beam is guided within the core material or scattered out of it. Here, θ_{c} is the angle between the normal to the interface of the core material and the cladding material and the incident beam, and θ_{s} is the corresponding angle for the substrate material. The refractive indices follow the relationship $n_{\text{c}} < n_{\text{f}}$ and $n_{\text{s}} < n_{\text{f}}$. For the condition of TIR to be fulfilled, and thus for the beam to be guided within the core material, the incident angle θ_{i} must satisfy $\theta_{\text{i}} > \theta_{\text{c}}$ and $\theta_{\text{i}} > \theta_{\text{s}}$ [6].

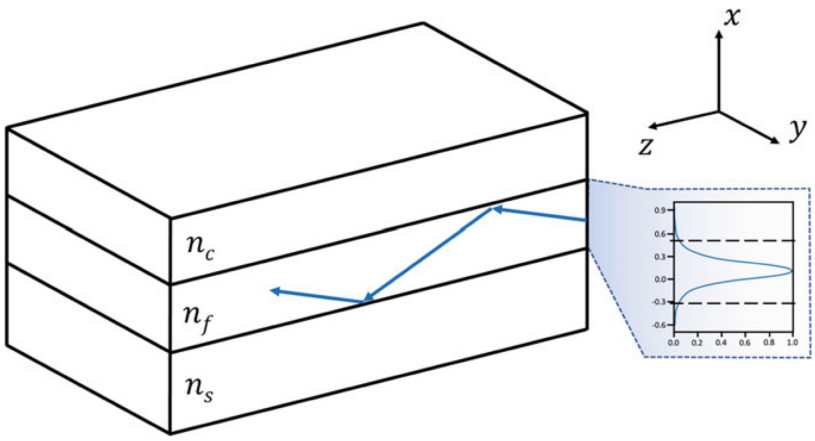

Figure 2: A schematic representation of a slab waveguide consisting of a core material (f), a substrate (s), and a cladding (c), figure taken from [6], chap. 3, p. 34.

2.1.2 Maxwell Equations Picture

In addition to describing the propagation of light using ray optics, light can also be described as an electromagnetic wave using Maxwell's equations. For this, the wave equation is derived from Maxwell's equations, and then the propagating modes, are described. In the following description, a harmonic time dependence of the wave propagating in the waveguide of the form $e^{i\omega t}$ is considered where i is the imaginary unit, ω is the angular frequency, and t is the time. The situation we want to describe here is again the one shown in figure 2. Under the described conditions, the curl equations of Maxwell's equations for the $\vec{E}$-field and the $\vec{H}$-field are,

$$\nabla \times \vec{E} = -i\omega\mu_0\vec{H} \tag{2.3}$$

$$\nabla \times \vec{H} = i\omega\epsilon_0 n^2\vec{E} \tag{2.4}$$

with the refractive index squared $n^2 \equiv \frac{\epsilon}{\epsilon_0}$ where ϵ is the permittivity of the material, ϵ_0 is the electric constant and μ_0 is the vacuum magnetic permeability [6]. By applying $\nabla\times$ to equation 2.3 and using the vacuum condition $\nabla \cdot \vec{E} = 0$, the wave equation for the $\vec{E}$-field,

$$\nabla^2\vec{E} + k^2n^2\vec{E} = 0 \tag{2.5}$$

is obtained, with the wavenumber $k = \omega\sqrt{\epsilon_0\mu_0}$ [6]. Due to the chosen geometry in the example, the waveguide is infinitely extended in the z-direction, al-

lowing modes to propagate in this direction. For forward-propagating modes, the z-dependence of the $\vec{E}$-field is $e^{-i\beta z}$ with the propagation constant β. Furthermore, in the given geometry, the allowed modes have wave vectors in the x and z directions, resulting in

$$k_x^2 + \beta^2 = n^2 k^2, \tag{2.6}$$

with k_x being the wavenumber in x-direction, from which the properties of the propagating modes can be determined [6].The effective wave velocity of the mode in the z-direction

$$v = \frac{ck}{\beta} = \frac{c}{n_{\text{eff}}} \tag{2.7}$$

depends on the effective refractive index n_{eff} and the speed of light c [6]. The effective refractive index accounts for changes in the wave's velocity that result from the material and the geometry of the material. For the guided modes,

$$n_{\text{c}} < n_{\text{eff}} < n_{\text{f}} \tag{2.8}$$

$$n_{\text{s}} < n_{\text{eff}} < n_{\text{f}} \tag{2.9}$$

holds true, with respect to the refractive indices of the cladding or the substrate material and the core material [6].
To describe the modes guided in the waveguide, an initial approach is made for the solutions of the $\vec{E}$- and $\vec{H}$-fields. Due to the considered symmetry the polarization and amplitude remain constant along the longitudinal z coordinate. Therefore,

$$\vec{E}_\nu(\vec{r}, t) = \vec{\mathcal{E}}_\nu(x, y) e^{i\beta_\nu z - i\omega t} \tag{2.10}$$

$$\vec{H}_\nu(\vec{r}, t) = \vec{\mathcal{H}}_\nu(x, y) e^{i\beta_\nu z - i\omega t} \tag{2.11}$$

applies, where ν is the mode index and $\vec{\mathcal{E}}_\nu(\vec{r}, t)$ and $\vec{\mathcal{H}}_\nu(\vec{r}, t)$ are the field distributions of the corresponding mode [7]. By applying the curl equations

of Maxwell's equations, and using the two equations 2.10 and 2.11 we get

$$\frac{\partial \mathcal{E}_z}{\partial y} - i\beta \mathcal{E}_y = i\omega\mu_0 \mathcal{H}_x, \qquad \frac{\partial \mathcal{H}_z}{\partial y} - i\beta \mathcal{H}_y = -i\omega\epsilon \mathcal{E}_x, \tag{2.12}$$

$$i\beta \mathcal{E}_x - \frac{\partial \mathcal{E}_z}{\partial x} = i\omega\mu_0 \mathcal{H}_y, \qquad i\beta \mathcal{H}_x - \frac{\partial \mathcal{H}_z}{\partial x} = -i\omega\epsilon \mathcal{E}_y, \tag{2.13}$$

$$\frac{\partial \mathcal{E}_y}{\partial x} - \frac{\partial \mathcal{E}_x}{\partial y} = i\omega\mu_0 \mathcal{H}_z, \qquad \frac{\partial \mathcal{H}_y}{\partial x} - \frac{\partial \mathcal{H}_x}{\partial y} = -i\omega\epsilon \mathcal{E}_z. \tag{2.14}$$

which can, in turn, be transformed into equations for the transverse electric and magnetic fields,

$$(k^2 - \beta^2)\mathcal{E}_x = i\beta \frac{\partial \mathcal{E}_z}{\partial x} + i\omega\mu_0 \frac{\partial \mathcal{H}_z}{\partial y} \tag{2.15}$$

$$(k^2 - \beta^2)\mathcal{E}_y = i\beta \frac{\partial \mathcal{E}_z}{\partial y} - i\omega\mu_0 \frac{\partial \mathcal{H}_z}{\partial x} \tag{2.16}$$

$$(k^2 - \beta^2)\mathcal{H}_x = i\beta \frac{\partial \mathcal{H}_z}{\partial x} - i\omega\epsilon \frac{\partial \mathcal{E}_z}{\partial y} \tag{2.17}$$

$$(k^2 - \beta^2)\mathcal{H}_y = i\beta \frac{\partial \mathcal{H}_z}{\partial y} + i\omega\epsilon \frac{\partial \mathcal{E}_z}{\partial x} \tag{2.18}$$

where in this case $k^2 = \omega^2\mu_0\epsilon(x, y)$ with the permittivity $\epsilon(x, y)$ [7].
In general, there are different solutions for guided modes, characterized by the fact that certain components of the $\vec{E}$- and $\vec{H}$-fields become zero [7]. We will consider the transverse magnetic (TM) and transverse electric (TE) modes. The distinction between these modes arises from the fact that in TE modes, the $\vec{E}$-field lies only in the plane parallel to the waveguide ($\mathcal{E}_z = 0$), whereas in TM modes, this is true for the $\vec{H}$-field ($\mathcal{H}_z = 0$). From Maxwell's equations, it follows that these two modes are independent of each other. In figure 3 the TE 0 mode is shown. Additionally, TM and TE modes differ from simple plane waves in that they have a component in the direction of propagation, for the TE mode, $\mathcal{H}_z \neq 0$, and for the TM mode, $\mathcal{E}_z \neq 0$ [6, 7].

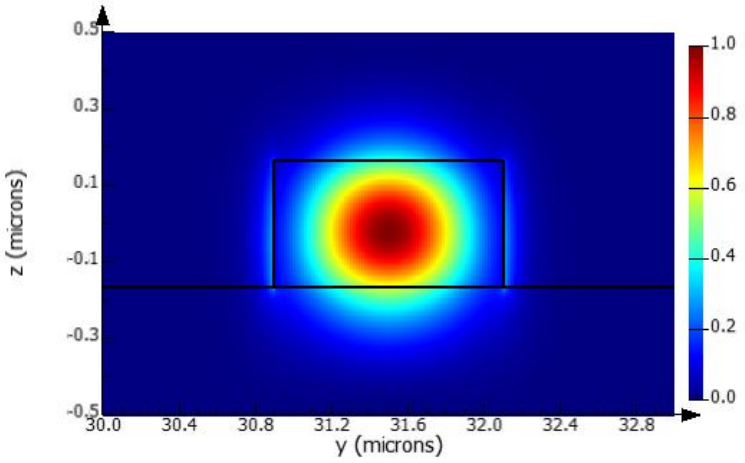

Figure 3: Simulation result for the distribution of the $\vec{E}$-field for the cross section of a waveguide of a Si_3N_4 waveguide on a Si_2O substrate. The TE 0 mode is shown here.

2.2 Directional Coupler

After discussing the most fundamental components of PICs, namely waveguides, this section will focus on directional couplers. These couplers will be used in the construction of the multiplexer, and their basic operating principle is also relevant for ring resonators and bragg gratings to be discussed later. Directional couplers are important components in integrated optics for splitting and combining light. They consist of two parallel waveguides in close proximity, allowing for transfer of optical power between them [8]. In figure 4, the basic structure of a directional coupler is shown. The operation

Figure 4: Illustration of a directional coupler with a length of 30 μm, a gap of 0.5 μm, a waveguide width of 1.2 μm and a bend radius of 30 μm.

of directional couplers is based on evanescent coupling, where the optical fields from each waveguide overlap and transfer power between them. The coupling of light between the waveguides can be rigorously described using

Maxwell's equations by solving them for the regions under consideration and the boundary conditions. However, this approach can be quite complex and computationally intensive. Therefore, we will use an approach called coupled mode theory [8].
The next section on coupled mode theory follows [8]. In coupled mode theory, the mode propagating in one of the two parallel waveguides is considered as if the other waveguide were not present. Thus, the spatial distribution and propagation constant of the mode remain unchanged, and only the amplitude $a_i(z)$ of the mode propagating in each waveguide varies. For the amplitudes,

$$\frac{\mathrm{d}a_1}{\mathrm{d}z} = -ic_{21} \cdot \exp(i\Delta\beta z) \cdot a_2(z) \tag{2.19}$$

$$\frac{\mathrm{d}a_2}{\mathrm{d}z} = -ic_{12} \cdot \exp(i\Delta\beta z) \cdot a_1(z) \tag{2.20}$$

applies. Here c_{21} and c_{12} are the coupling coefficients and $\Delta\beta$ is defined as $\Delta\beta = \beta_1 - \beta_2$. The equations 2.19 and 2.20, as coupled second-order differential equations, have the general solution

$$a_1(z) = A(z)a_1(0) + B(z)a_2(0) \tag{2.21}$$

$$a_2(z) = C(z)a_1(0) + D(z)a_2(0) \tag{2.22}$$

where the coefficients of the solution are given by

$$A(z) = D^*(z) = \exp\left(\frac{i\Delta\beta z}{2}\right)\left[\cos\gamma z - i\frac{\Delta\beta}{2\gamma}\sin\gamma z\right] \tag{2.23}$$

$$B(z) = \frac{c_{21}}{i\gamma}\exp\left(\frac{i\Delta\beta z}{2}\right)\sin\gamma z \tag{2.24}$$

$$C(z) = \frac{c_{12}}{i\gamma}\exp\left(-\frac{i\Delta\beta z}{2}\right)\sin\gamma z. \tag{2.25}$$

These coefficients are the elements of a transfer matrix $\mathbf{T}$. Furthermore, γ and c are defined as

$$\gamma^2 = \left(\frac{\Delta\beta}{2}\right)^2 + c^2, \quad c = \sqrt{c_{12}c_{21}}. \tag{2.26}$$

The power in each respective waveguide is proportional to the squared amplitude. Therefore, in the case where no light is initially emitted into the second waveguide, the following equations for the power in the waveguides

arise. It becomes apparent that the power $P_{\mathrm{i}}(z)$ in the respective waveguides,

$$P_1(z) = P_1(0)\left[\cos^2\gamma z + \left(\frac{\Delta\beta}{2\gamma}\right)^2 \sin^2\gamma z\right] \tag{2.27}$$

$$P_2(z) = P_1(0)\left[\frac{|c_{21}|^2}{\gamma^2}\sin^2\gamma z\right] \tag{2.28}$$

oscillates periodically between the two waveguides. If it is further assumed that the waveguides are identical in all their properties that is, the refractive indices n_{i}, the propagation constants β_{i}, as well as the coupling coefficients c_{ij}, the equations simplify even further. Thereby showing the periodic transfer of power,

$$P_1(z) = P_1(0)\cdot\cos^2 cz \tag{2.29}$$

$$P_2(z) = P_1(0)\cdot\sin^2 cz \tag{2.30}$$

between the waveguides clearly. With a directional coupler, it is thus possible to couple a certain portion of the optical power from one waveguide to another, depending on the length of the coupling region of the directional coupler [8]. In figure 5, the oscillation of the electric field within the coupling region of a directional coupler is schematically illustrated.

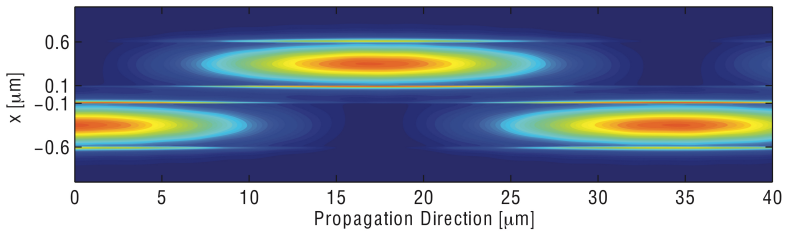

Figure 5: Propagation of the $\vec{E}$-field in a directional coupler, figure taken from [9], chap. 4, p. 95.

In addition to the length of the coupling region, the gap between the two waveguides is also crucial for the transfer of optical power. The gap influences the coupling coefficient, which decreases exponentially as the gap increases [9]. To calculate the distance at which the optical power is completely transferred from one waveguide to the other, the entire electric field $E_{total}(r)$ present in both waveguides must be considered. This field consists of two different field components $E_1(x, y)$ and $E_2(x, y)$ with different propagation

constants β_1 and β_2. Resulting in

$$E_{\text{total}}(r) = \tilde{A}(0)\left[E_1(x,y)e^{i\beta_1 z} + E_2(x,y)e^{i\beta_2 z}\right]. \tag{2.31}$$

These respective modes are called supermodes. When there is a phase shift of π between these two supermodes, the power transfer is maximal. In the case of a symmetric directional coupler with identical waveguides, the supermodes can be referred to as even E_{even} and odd E_{odd} modes [7].
Lastly, it is interesting to examine how the power fraction coupled between the two waveguides depends on the length of the directional coupler. The fraction of power coupled from one waveguide to the other is denoted by κ^2, while the fraction remaining in the original waveguide is denoted by t^2. Here

$$\kappa^2 = \sin^2(C \cdot L) \tag{2.32}$$
$$t^2 = \cos^2(C \cdot L) \tag{2.33}$$
$$t^2 + \kappa^2 = 1 \tag{2.34}$$

apply, with $C = \frac{\pi\Delta n}{\lambda}$, where Δn is the difference in the effective refractive indices of the even and odd modes, and L is the length of the directional coupler [9]. Using these formulas, we can now provide a general expression for how long the directional coupler must be to couple a specific fraction of power from one waveguide to the other. Leading to

$$L = \frac{\arcsin(\kappa)\lambda}{\pi\Delta n}. \tag{2.35}$$

The coupling length at which the total optical power is transferred from one waveguide to the other one L_c can be calculated as

$$L_c = \frac{\pi}{\beta_{\text{even}} - \beta_{\text{odd}}}, \tag{2.36}$$

with the propagation constants for the two different modes being determined through simulations which will be described later on in more detail [7].

2.3 Ring Resonator

Ring resonators represent one of the two fundamental building blocks required for our multiplexer. These consist of a waveguide in a ring or racetrack shape and, depending on the configuration, one or two straight waveguides. The purpose of the used ring resonator for this application is to achieve a wavelength selective transmission of light from one waveguide to another with

minimal loss, while being very precise with respect to the wavelength [9]. In figure 6, the two most common types of ring resonators are depicted.

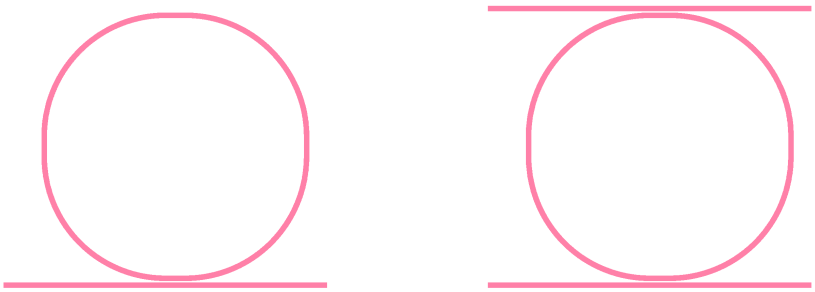

Figure 6: Illustration of two ring resonators. On the left, an all-pass ring resonator, and on the right, an add-drop ring resonator. Both are racetrack ring resonators with a horizontal and a vertical straight region. The dimensions here are: waveguide width = 1.2 μm, resonator radius = 30 μm, gap = 0.5 μm, and straight length = 5 μm (horizontal and vertical).

The general operating principle of a ring resonator is based on the coupling of light from a waveguide onto a ring. This happens in the region where the ring and the waveguide come closest together, effectively creating a directional coupler. On the ring light circulates and undergoes constructive or destructive interference depending on the wavelength, thus creating a resonance condition [9]. For the light to constructively interfere with itself after a round trip, the resonance condition is that the phase θ acquired in one round trip fulfills $\theta = 2\pi m$, with $m \in \mathbb{N}$. Therefore, the optical length of the ring must be a multiple of the resonant wavelength, for light to resonate on the ring. This relationship is represented in,

$$\lambda_{\text{res}} = \frac{n_{\text{eff}} L}{m} \tag{2.37}$$

where $m \in \mathbb{N}$ and L is the length of the ring [10].
The most basic form of the ring resonator is the all-pass ring resonator, which is shown on the left side of figure 6. The all-pass ring resonator consists of a curved waveguide that forms the ring and a straight waveguide located near this ring. At the mentioned region that forms a directional coupler, light that meets the resonance condition can couple onto the ring. Figure 7 shows the coupling region of the all-pass ring resonator between the ring and the waveguide. The cross-over coupling coefficient $-\kappa^*$ describes how much light is coupled into the ring, while the through coefficient t represents how much light remains in the straight waveguide. κ describes how much light is

coupled out of the ring, and t^* is the fraction of light that is not coupled out and remains in the ring.

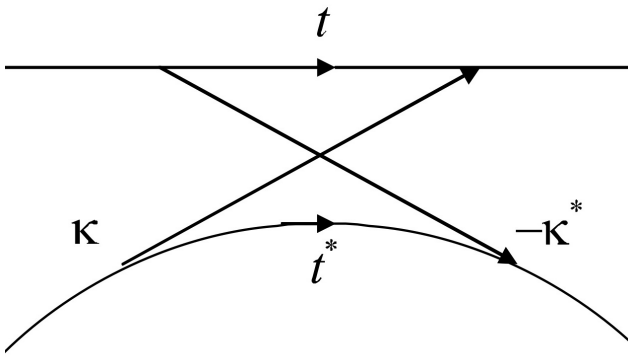

Figure 7: The coupling region of the all-pass filter, including all key parameters, figure taken from [11], p. 4.

The ring resonators that will be used for the multiplexer are called add-drop ring resonators. As shown on the right side of figure 6, these have an additional waveguide near the ring resonator that is parallel to the existing one. We will focus on this configuration in the following discussion, because the resonance can be exploited to only transfer the resonant wavelength to the multiplexer output, whereas in the all-pass ring resonator, the resonant light reaches the through port with a weak intensity [10].
Figure 8 provides a schematic representation of a ring resonator in the add-drop configuration, indicating all the properties used for mathematical explanation. For the description of the amplitudes of light at the individual ports of the ring resonator, the amplitude of the light at the input port is initially set to $E_{i1} = 1$. This yields

$$E_{t1} = t_1 + \frac{-\kappa_1\kappa_1^* t_2^* \alpha_{1/2}^2 e^{i\theta}}{1 - t_1^* t_2^* \alpha_{1/2}^2 e^{i\theta}} \overset{|\kappa_1|^2+|t_1|^2=1}{=} \frac{t_1 - t_2^* \alpha e^{i\theta}}{1 - t_1^* t_2^* \alpha e^{i\theta}} \tag{2.38}$$

$$E_{t2} = \frac{-\kappa_1^* \kappa_2 \alpha_{1/2} e^{i\theta_{1/2}}}{1 - t_1^* t_2^* \alpha e^{i\theta}} \tag{2.39}$$

for the amplitudes at the throughput port E_{t1} and the drop port E_{t2} [11]. Here, t_1, t_2, κ_1, and κ_2 are the straight-through and cross-over coupling coefficients of the input and drop couplers with * denoting the complex conjugated

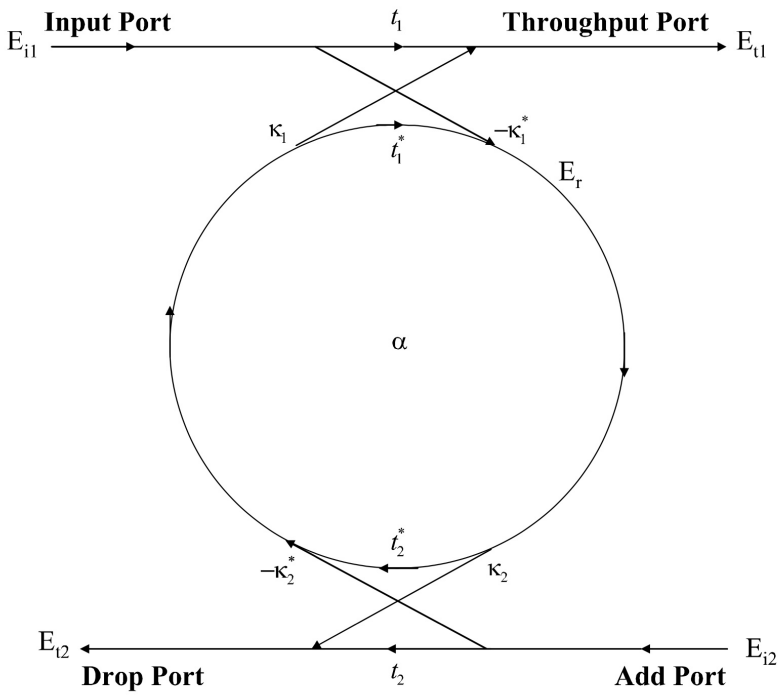

Figure 8: Add-drop ring resonator including the key properties and labels used for mathematical characterization, figure taken from [11], p. 7.

values. Furthermore, α and $\alpha_{1/2}$ represent the remaining amplitude after a round trip and after half a round trip, respectively. With an ideal ring having zero loss $\alpha = 1$.
$\theta = \frac{4\pi^2 r n_{\text{eff}}}{\lambda}$ is the phase accumulated over a round trip (with r being the ringradius), and $\theta_{1/2}$ is the phase accumulated over half a round trip. It holds that $\alpha = (\alpha_{1/2})^2$ and $\theta = 2\theta_{1/2}$ [11].
In a symmetric and lossless ring resonator, i.e., one with $t_1 = t_2$ and $\alpha = 1$,

$$E_{t1} = \frac{t - t^* \cdot 1 \cdot e^{i \cdot 2\pi m}}{1 - t^* t^* \cdot 1 \cdot e^{i \cdot 2\pi m}} = 0 \qquad \text{with: } m \in \mathbb{Z} \tag{2.40}$$

applies for the field at the throughput port at a resonance wavelength, with $\theta = 2\pi m$. This occurs because the transmission coefficients are equal to their complex conjugates, resulting in the numerator being zero. Since the ring is lossless in this scenario, the entire field amplitude would be measured at the drop port. The spectrum would appear as in figure 9 in this case [11].
Using the amplitude of the E-field at the respective port, the transmission of the intensity of the E-field can also be determined by squaring the am-

plitude and normalizing it by the squared amplitude of the input port. For our application, the transmission at the drop port is particularly important. Here, in combination with the resonance condition,

$$T_{t1,max} = \frac{(1-t_1^2)(1-t_2^2)\alpha}{(1-t_1 t_2 \alpha)^2} \tag{2.41}$$

applies for the general case with different coefficients t_1 and t_2 for the maximal transmission [10].

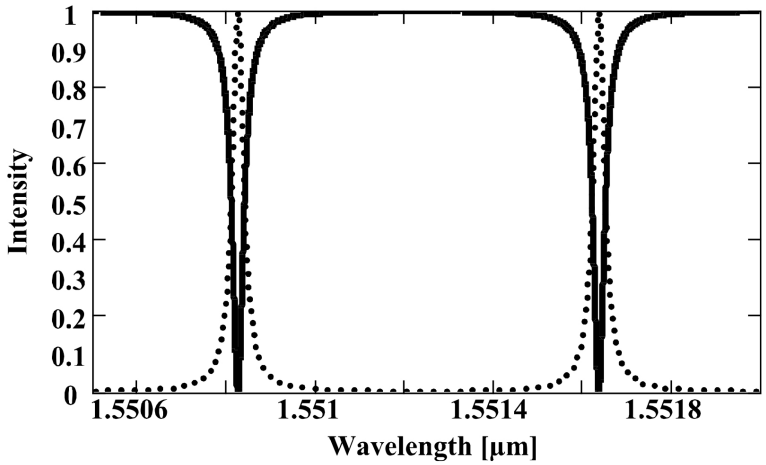

Figure 9: Ideal spectrum for an add-drop ring resonator. The spectrum measured at the throughput port is indicated by the solid line, and the spectrum at the drop port is indicated by the dashed one, figure taken from [11], p. 8.

In reality, the ring resonator is not lossless, so the spectrum shown is not achieved. The optimal parameters for the ring will be determined in the following chapters through experimental parameter sweeps based on simulations and experimental data.
The key properties of a ring resonator that will later be characterized are discussed in the following. One of the principal properties of ring resonators is the Free Spectral Range (FSR). The FSR is the wavelength separation between the m-th and the $m+1$-th resonance wavelengths, as given in equation 2.37.

$$\mathrm{FSR} = \frac{\lambda_{\mathrm{res}}^2}{n_{\mathrm{g}} L}, \tag{2.42}$$

where λ_{res} is the resonance wavelength, n_{g} is the group index, and L is the circumference at the center of the waveguide of the ring [11]. Another signif-

icant property is the Full Width at Half Maximum (FWHM). The FWHM specifies the bandwidth of the resonance peak at half its maximum intensity. It is defined as

$$\text{FWHM} = \frac{(1 - t_1 t_2 \alpha)\lambda_{\text{res}}^2}{\pi n_{\text{g}} L \sqrt{t_1 t_2 \alpha}}. \tag{2.43}$$

This means that with a small FWHM, the peaks are very sharp, and conversely, with a larger FWHM, they are broader [10]. The Q-factor is a measure of the resonator's efficiency. This indicates the number of round trips the light completes in the ring before being lost due to internal attenuation. Here

$$Q = \frac{\lambda_{\text{res}}}{\text{FWHM}} \tag{2.44}$$

applies. A higher Q-factor corresponds to a narrower FWHM, implying lower losses and better performance. The Q-factor is defined as shown below [10]. A parameter that is closely related to the Q-factor is the finesse F, where

$$F = \frac{\text{FSR}}{\text{FWHM}} \tag{2.45}$$

holds true. It is also a measure of the sharpness of the resonance peaks [11]. The last important property of the ring resonator for us is the Extinction Ratio (ER). At the drop port, the ER is defined as the peak transmission versus the one at the drop port off-resonance, while at the through port, it is measured as the depth of the dip versus the input signal. The ER is calculated from the intensities at the different ports, which are the squares of the E-field amplitude. For the extinction ratio of the drop port transmission

$$\text{ER} = \frac{(1 + t_1 t_2 \alpha)^2}{(1 - t_1 t_2 \alpha)^2} \tag{2.46}$$

applies [10].

2.4 Bragg Grating

Bragg Gratings are the second fundamental building block for the multiplexer. First, the operation of a single Bragg grating will be examined, followed by the specific configuration of Bragg filters used in the construction of the multiplexer [9]. In figure 10 a bragg grating is shown. Characteristic for this structure is that the effective refractive index is periodically varied. Since the effective refractive index of a material is depends also on its geometry [6], this can be achieved by varying the cross-sectional dimension of the waveguide orthogonal to the direction of light propagation. Alternatively, the

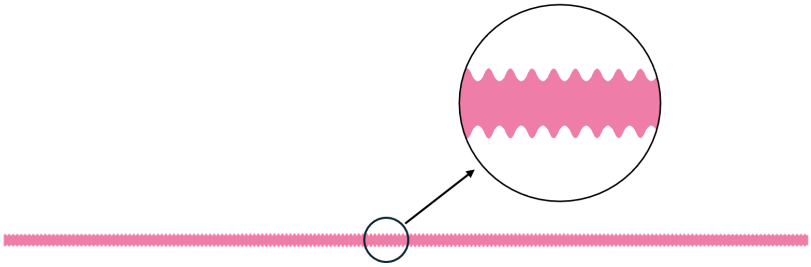

Figure 10: Illustration of a Bragg grating, where the periodic structure of this grating can be clearly seen in the close-up view. The dimensions here are periodicity = 0.5 μm resonance width = 5 nm and gratings = 200.

material itself could be periodically altered, although this is more challenging to fabricate. Within the Bragg grating, partial reflections of the light occur at each interface. The relative phase of the reflected light depends on the wavelength and the period of the grating. This leads to multiple reflections within the grating, where the reflected signals only constructively interfere within a specific wavelength range. For the remaining light, the reflections interfere destructively, allowing this light to be transmitted through the filter. In figure 11 the structure of a Bragg grating is shown and in figure 12 the transmission and reflection spectra are depicted [9].

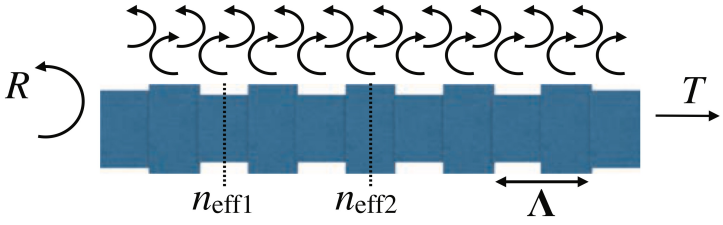

Figure 11: Schematic representation of a Bragg grating with two effective refractive indices $n_{\text{eff i}}$ and the grating period Λ as well as the transmission T and reflection R figure taken from [9], p. 118.

In the description of the Bragg gratings, two specific properties are particularly interesting for the construction of the multiplexer: the central wavelength λ_{B} and the bandwidth of the Bragg grating in which the wavelengths are reflected $\Delta\lambda$. The central wavelength of the reflected range of the Bragg grating,

$$\lambda_{\text{B}} = 2\Lambda n_{\text{eff}} \tag{2.47}$$

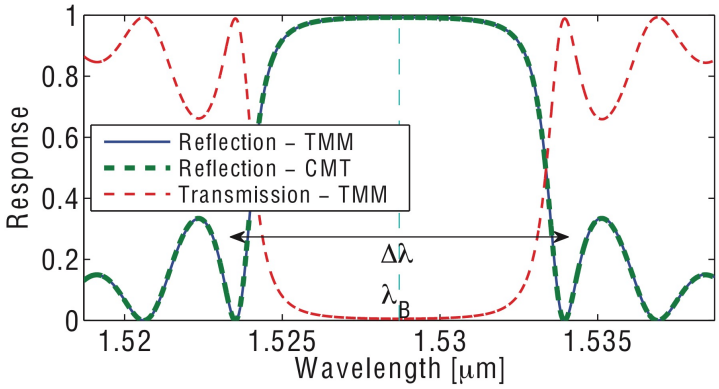

Figure 12: Simulations using the Transfer Matrix Method (TMM) and Coupled Mode Theory (CMT) for the transmission and reflection spectrum for a Bragg reflector with a center wavelength of 1529 nm, figure taken from [9], p. 118.

can be calculated from the average effective refractive index n_{eff} as well as the grating period Λ [9]. For the band gap in transmission,

$$\Delta\lambda = \frac{\lambda_{\text{B}}^2}{\pi n_{\text{g}}} \sqrt{\kappa^2 + \left(\frac{\pi}{L}\right)^2} \tag{2.48}$$

applies, where n_{g} is the group index, κ is the coupling coefficient indicating the strength of reflection per unit length and L is the length of the Bragg grating. Here, $\Delta\lambda$ is defined as the width between the first minima on the left and right of the central wavelength. The central wavelength is primarily influenced by the average effective refractive index and the periodicity. While the periodicity can be set during the design phase, the effective index n_{eff} depends on the material used and the precise geometry of the grating. The bandwidth of the Bragg filter is determined by the group index, which is also dependent on the material and geometry, as well as the wavelength [9].

2.4.1 Bragg Filter

The following section discusses the Bragg filters used in the multiplexer, which consist of Bragg gratings and directional couplers. Functionally they are also an add-drop structure, as they feature an input port, a drop port, a through port, and an add port. However, they differ from add-drop-ring resonators in the reflected spectra [12]. The structure is shown in figure 13. In the arrangement shown in figure 13, the signal to be filtered enters the Bragg filter at the input port (Port 1). At Coupler 1, the signal is split in

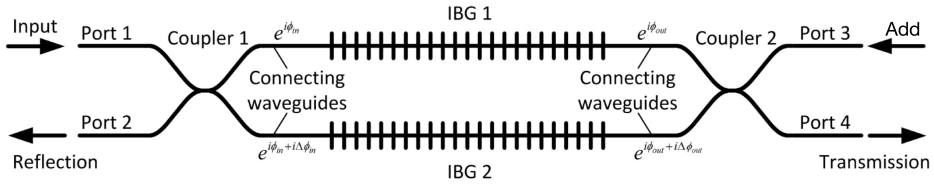

Figure 13: Representation of the Bragg filters with their functionality. In this case, the couplers are directional couplers with integrated Bragg gratings (IBG) at their ends. Additionally, the phase of the light is indicated at the waveguides, figure taken from [12], p. 16665.

a 50:50 ratio, directing half of the light towards IBG 1 and the other half towards IBG 2. When the light is coupled in Directional Coupler 1 from the upper waveguide to the lower waveguide, a phase shift occurs, denoted as $i\Delta\phi_{in}$ in the figure, corresponding to a phase shift of $\pi/2$. During propagation in the Bragg gratings, a specific wavelength range of the light is reflected, while the rest is transmitted, as described. Since the light in the two identical IBGs accumulates an identical phase, the change in this phase, being the same for the light in the upper and lower waveguides, does not need to be examined in detail to understand the functionality of the Bragg-Filter [12].
The following explanation describes the path of light that undergoes constructive interference and the path of light that undergoes destructive interference.
First, we consider the path leading to constructive interference. The light reflected in IBG 1 propagates towards Coupler 1 from the right. Upon reaching Coupler 1, the reflected light is split in a 50:50 ratio where the light coupled towards Port 2, receives a phase shift of $\pi/2$. Simultaneously, the light reflected from IBG 2 which after the splitting continues towards Port 2 has also a phase shift of $\pi/2$ by coupling from the input port into the lower waveguide through the directional coupler. As a result, the light at Port 2 coming from both IBGs is in phase and interferes constructively, leading to a strong reflected signal at this port [12].
Next, we describe the constructive interference for the light transmitted through the Bragg gratings. This light propagates towards Coupler 2, where it is split evenly in a 50:50 ratio between the two waveguides. The light from IBG 1, after being coupled through Coupler 2, continues towards Port 4 with a phase shift of $\pi/2$. Meanwhile, the light from IBG 2, which has not undergone further coupling in Coupler 2, also propagates towards Port 4 with the phase shift of $\pi/2$ which it got from the coupling in Coupler 1. Since both light waves from IBG 1 and IBG 2 are in phase, constructive interference occurs at Port 4 (the transmission port) [12].

Conversely, for destructive interference, consider the light paths that lead to Port 1 and Port 3. At Port 1, the light reflected from IBG 1 which has undergone no phase shift interferes with the light reflected in IBG 2, which has undergone a $\pi/2$ phase shift when coupling from the upper to the lower waveguide and an additional $\pi/2$ phase shift when coupling back to the upper waveguide, resulting in a total phase shift of π. Thus, at this port, light with a π phase shift interferes with light that has no phase shift. As a result, the two light waves interfere destructively, minimizing the signal at this port [12].
Similarly, at Port 3 (the add port), the light from the upper waveguide, which experiences no phase shift, interferes with the light from the lower waveguide, which has undergone a π phase shift due to the coupling in Coupler 1 and in Coupler 2. This phase difference causes destructive interference and thus minimal transmission. Despite this, Port 3 can still function as an add port for wavelengths outside the reflected spectrum, allowing these signals to reach Port 2 [12]. The phase relationships of the light are summarized in formulas 2.49 to 2.52:

$$\text{Input-port (Port 1)}: e^{i\phi_{out_1}} + e^{i\phi_{out_1}+i\pi/2+i\pi/2} = 0 \tag{2.49}$$

$$\text{Reflection-port (Port 2)}: e^{i\phi_{out_1}+i\pi/2} + e^{i\phi_{out_1}+i\pi/2} \neq 0 \tag{2.50}$$

$$\text{Add-port (Port 3)}: e^{i\phi_{out}} + e^{i\phi_{out}+i\pi/2+i\pi/2} = 0 \tag{2.51}$$

$$\text{Transmission-port (Port 4)}: e^{i\phi_{out}+i\pi/2} + e^{i\phi_{out}+i\pi/2} \neq 0 \tag{2.52}$$

Here, ϕ_{out_1} represents the phase of the light at port 1 and port 2. However, this phase differs from the phase ϕ_{out} at ports 3 and 4, as the light travels a different path. Compared to a simple Bragg grating, the Bragg filter offers the advantage of having two additional ports, which broadens its application potential. In a simple Bragg grating, the input port and the reflection port are the same, and there is no add port like in the Bragg filter [12].

3 Methods

In this section, a design proposal for the multiplexer is first discussed. Based on this, the simulations necessary for determining the parameters for the ring resonators and the Bragg Filters are examined, as well as the programs required for these simulations. Finally, the measurement setup, where the measurements are conducted, is discussed. In figure 14, the platform on which the simulations are conducted and upon which the chips are later built and measured is shown. The figure depicts the simplest structure, namely the cross-section of a waveguide. For our application, we use Si_3N_4 as the material for the waveguides, as it has very low losses and fabrication steps are well understood, with established recipes [13].

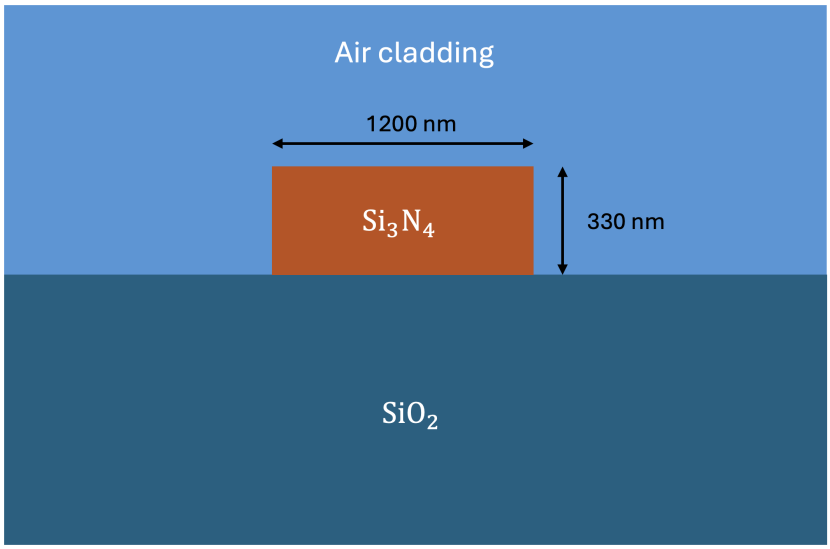

Figure 14: Cross-section of the used Si_3N_4 waveguide on SiO_2 with Air cladding for the dimensions of the waveguide.

3.1 Multiplexer Design

This section presents a design proposal for a multiplexer, highlighting the approach and required optimisation. An image of the entire multiplexer is provided in figure 15.
The multiplexer chip is designed for a setup with 20 lasers ranging from 1550 nm to 1569 nm, while the lasers are spaced one nm apart in terms of wavelength. Each laser has an associated ring resonator on the chip, whose through port signal can be returned to photiodes on the sender chip for mon-

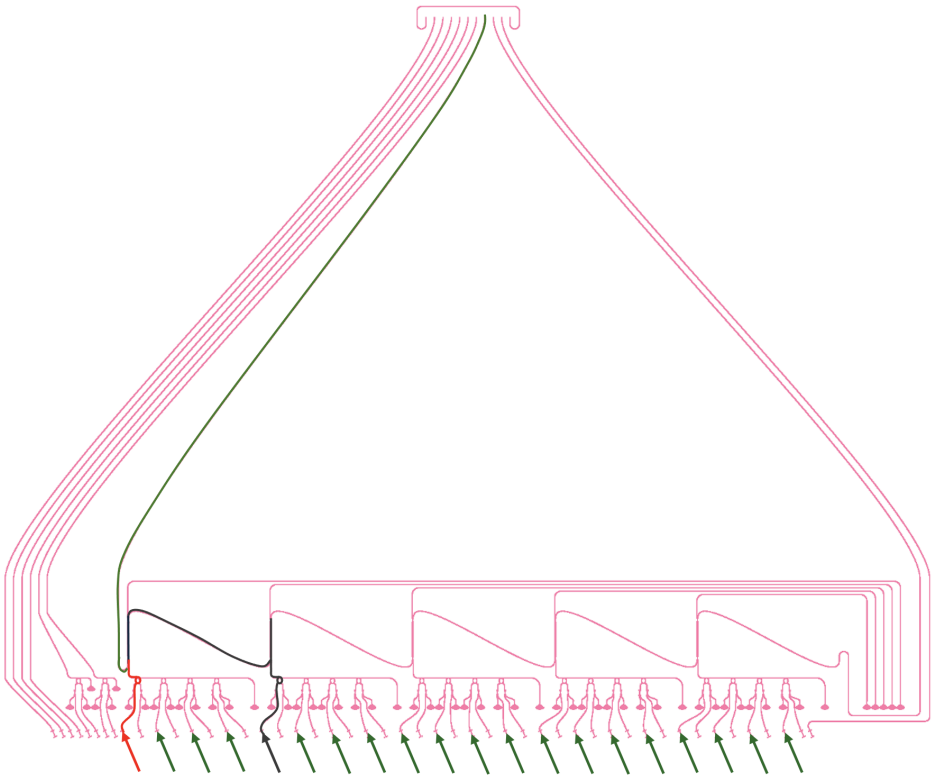

Figure 15: Depiction of the whole multiplexer. The 20 parallel arrows at the bottom of the image indicate where the light from the 20 lasers is coupled onto the multiplexer. For the coupling, polymer lens couplers are used [14]. Two paths for the laser light are illustrated as examples of how the multiplexer operates, one in red and one in dark blue, both leading to the waveguide for the multiplexed signal, shown in green.

itoring. The polymer lens couplers [14], which are later printed onto the chip, are positioned to achieve optimal coupling from the output of the sender chip onto the multiplexer chip.
A notable feature of the multiplexer is that it is modular, composed of individual cells, each consisting of four ring resonators and one Bragg filter. This design allows the multiplexer to be scaled to any size with minor adjustments, by adding or removing these modules as needed. A close-up image of such a module is shown in figure 16. In the bottom row in figure 16, light is coupled in from the bottom-left polymer lens coupler into every second coupler. The light of two adjacent lasers, differs in wavelength by one nm. The directional couplers have a splitting ratio of 90:10, ensuring that 90% of the light remains in the waveguide and is coupled to the ring, the 10% are used

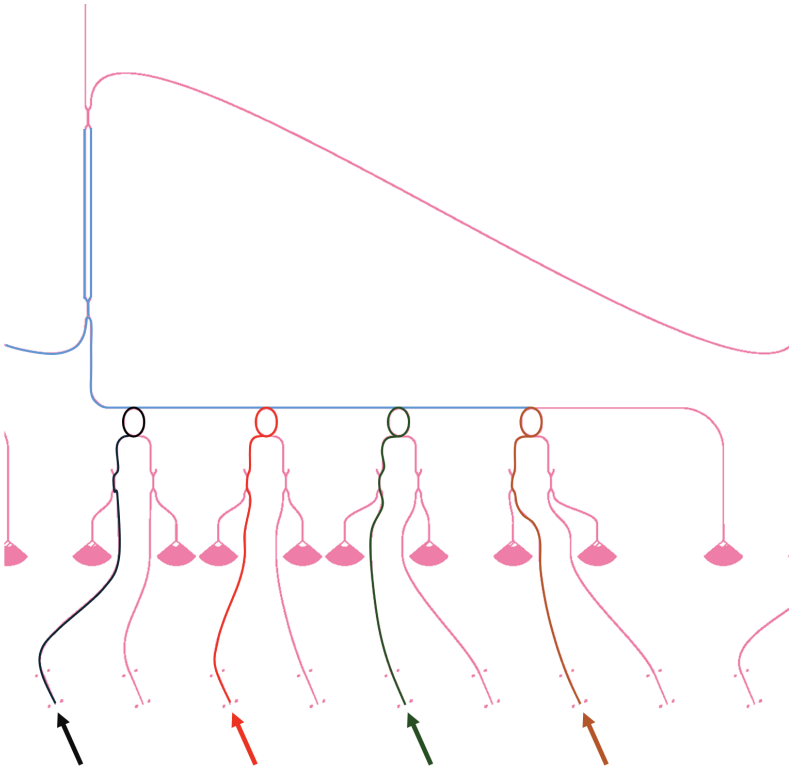

Figure 16: Illustration of a modular cell in the multiplexer, showing four ring resonators and a Bragg filter. The four arrows indicate where the laser light is coupled in and the path it takes through the ring resonators to the common waveguide in blue towards the Bragg filter. The signal reflected by the Bragg filter is shown also in blue on the left.

for calibrating and optimizing the rings to the right wavelength using silicon implantation and thermal tuning [13] before the polymer couplers are added. The Bragg filter is designed to reflect light within the wavelength range of the four ring resonators and transmit the rest. Thus, the light from the four lasers propagates through the common upper waveguide. It then enters the in port of the Bragg filter and is reflected to the drop port of the Bragg filter directly to its left. Using the add port, which is diagonally opposite the drop port, light from another module with four lasers having different wavelengths than those in the current module can also be transferred to the drop port, as the Bragg filter does not reflect light in that wavelength range. The upper row of grating couplers in figure 16, are perfectly parallel to the vertical axis, and will used to test and precisely characterize the ring resonators.
The design with four ring resonators was chosen because, due to the length

of the ring resonators, their FSR cannot be larger than four to five nm. The length of the rings must be sufficient to ensure good reproducibility, which will be discussed in section 4.1.1. Furthermore, rings with too small bending radii experience very high losses and they need to include the straight sections, visible in figure 18, so that the rings can later be precisely doped with silicon to a specific wavelength. The problem with building more than four rings, each with a resonance wavelength separated by one nm, onto a single waveguide with a four nm FSR would be that there is the risk that the light which should be multiplexed, could be coupled back out of the output waveguide by the other resonators. By using Bragg filters in the design, this issue can be avoided, as these filters reflect light within a specific wavelength range and transmit all other wavelengths. Due to the design of the multiplexer, when investigating the ring resonators and the Bragg filters, the resonance wavelength and the FSR for the ring resonators, as well as the Bragg wavelength and the bandwidth for the Bragg filters, are crucial to determine precisely.
Since the sender chip for which the multiplexer is being designed does not yet exist at the time of this work, the multiplexer was designed with parameters that can still be adjusted for the final chip.

3.2 Simulations

It is necessary to precisely determine the FSR and the resonance wavelength of the ring resonators. Additionally, the coupling between the ring and the waveguide must also be accurately determined. The design also requires that the central wavelength and bandwidth of the Bragg filters be correctly specified. Therefore, we will first discuss two simulation methods that will be used to conduct the simulations for the mentioned parameters. Subsequently, the simulations for the various parameters are explained.

3.2.1 Eigenmode Solver

Using the eigenmode solver simulation software, the propagating modes can be calculated for cross-sections with diverse geometries. This method is used in the thesis to determine the mode profiles, effective indices, and propagation constants for various waveguide configurations [9].
The eigenmode solver calculates the mentioned parameters by solving the time-invariant Maxwell equations in the frequency domain for the respective geometry. Various computational algorithms are used for this purpose. In our case, the simulation was performed using the computational algorithm Finite-Difference Eigenmode (FDE) which is included in the softwaresuite

Ansys Lumerical 2020 R2.4. The program allows the creation of the waveguide structure to be examined on a graphical user interface and subsequently enables the selection of the cross-section where the method should be applied. With the FDE method, the cross-section of the waveguide structure is first divided into equal-sized rectangular subsections using a spatial mesh. Then, in each of the individual mesh cells, Maxwell's equations are solved, formulated as a matrix eigenvalue problem. This results in the mode profiles, the modes, the effective indices and the group indizes of the waveguide structure. The accuracy of the simulation depends on the size of the cells in the mesh: the smaller the individual cells, the more precise the result. Although the finer the mesh, the more computationally intensive the calculations become for the computer [15].

3.2.2 Finite Difference Time Domain (FDTD)

One method for simulating the propagation of light in a medium is the Finite Difference Time Domain (FDTD) method. This method solves Maxwell's equations in the time domain by formulating the equations as difference equations, which can then be solved using numerical methods. The algorithm for this is known as the Yee algorithm [16]. The rotational equations of Maxwell's equations are first expanded, resulting in six equations for the time derivatives of the $\vec{E}$- and $\vec{H}$-fields for each spatial component. These are shown below [6].

$$\frac{\partial E_x}{\partial t} = \frac{1}{\epsilon_0}\left(\frac{\partial H_z}{\partial y} - \frac{\partial H_y}{\partial z}\right) \qquad \frac{\partial H_x}{\partial t} = \frac{1}{\mu_0}\left(\frac{\partial E_y}{\partial z} - \frac{\partial E_z}{\partial y}\right) \tag{3.1}$$

$$\frac{\partial E_y}{\partial t} = \frac{1}{\epsilon_0}\left(\frac{\partial H_x}{\partial z} - \frac{\partial H_z}{\partial x}\right) \qquad \frac{\partial H_y}{\partial t} = \frac{1}{\mu_0}\left(\frac{\partial E_z}{\partial x} - \frac{\partial E_x}{\partial z}\right) \tag{3.2}$$

$$\frac{\partial E_z}{\partial t} = \frac{1}{\epsilon_0}\left(\frac{\partial H_y}{\partial x} - \frac{\partial H_x}{\partial y}\right) \qquad \frac{\partial H_z}{\partial t} = \frac{1}{\mu_0}\left(\frac{\partial E_x}{\partial y} - \frac{\partial E_y}{\partial x}\right) \tag{3.3}$$

As with the eigenmode solver, a grid is used here to partition space into uniformly sized rectangular cuboid cells; similarly to the algorithm this grid is refered to as the Yee grid. Starting from an initial field distribution within the simulated area, the FDTD method computes the three vectors of the $\vec{E}$-field at each cell at that particular time. Subsequently, according to the equations shown in 3.1 to 3.3, the $\vec{H}$-field is calculated. This process is then either continued for a specified period or halted when the field reaches a certain minimal value, at which point the simulation is terminated. Using this method, unlike solving the wave equation, the coupling of the electric and magnetic fields can be taken into account directly [6].

3.2.3 Free Spectral Range

The Free Spectral Range 2.42, indicates the spacing between the resonance frequencies of the ring resonator. For the multiplexer designed in this thesis, it is required that the ring resonators have a FSR of at least 4 nm. The necessity of this requirement is due to to design of the multiplexer. The parameter that must be determined for the calculation of the FSR according to equation 2.42 is the group index n_g. This index depends on the wavelength, the respective materials and the waveguide geometry. It can be calculated using the eigenmode solver. The data for the material's refractive index as a function of wavelength is taken from [17] and was used here and also for other simulations. This was carried out using Lumerical's eigenmode solver in the wavelength range relevant for the multiplexer, i.e., in the range of 1550 nm to 1570 nm. Here the $\vec{E}$-field distributions across the waveguide cross-section were simulated for different wavelengths, allowing for the determination of both the effective refractive index and the group index.

3.2.4 Coupling Length and Gap

When determining the coupling length and gap of the ring resonator, the goal is to achieve a precise resonance frequency and high transmission of light at the desired resonance frequency. To describe the coupling of light between the waveguides at the ring resonator and the ring itself, the coupling regions at the top and bottom of the ring are first considered as directional couplers. The coupling region of the ring resonator differs from the directional coupler shown in figure 4 in that it is not a symmetrical component. The directional coupler is formed by the ring coming very close to the waveguide at one point, with high coupling between the waveguide and the ring also occurring in the regions around this closest point. To determine the coupling between the waveguide and the ring, 2.35 is used. For this, the eigenmode solver is also employed to simulate the effective refractive indices for the odd and even modes. In figure 17, the $\vec{E}$-field distribution in the eigenmode solver for two parallel waveguides is shown. The propagation of light with varying coupling strengths onto the ring was analyzed through FDTD simulations, enabling the simulation of light transmission as a function of wavelength for different gap sizes.

3.2.5 Resonance Wavelength

When determining the resonance wavelength, 2.37 is used. However, the effective refractive index of the ring resonator must first be determined. The ring resonator used for the multiplexer essentially consists of three sections

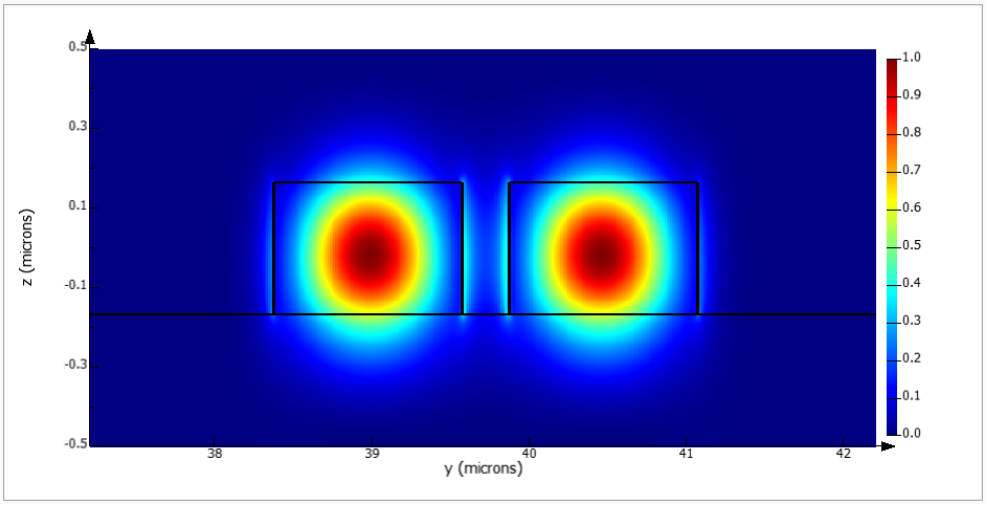

Figure 17: Example of the representation of a simulation result for the $\vec{E}$-field from the eigenmode solver for a cross-section of two parallel Si_3N_4 waveguides on a Si_2O substrate and air cladding with the dimensions shown in figure 14. The cross-section shows the mode profile for light with a wavelength of 1550 nm.

that have different refractive indices. These sections are shown in figure 18. The sections include, firstly, the curved parts of the ring resonator, secondly, the straight waveguides on the side of the ring resonator, and thirdly, the parts of the ring resonator in the coupling region. The sum of the respective coupling, curved, or straight parts is subsequently denoted as L_{bend}, L_{coupling}, and L_{straight}. To determine a theoretical value for the resonance wavelengths of the ring resonator, the wavelength-dependent effective refractive indices for the respective regions were again identified through simulations using the eigenmode solver. Subsequently, an effective refractive index for the entire ring was calculated, with the refractive indices of the individual regions weighted according to their proportions of the total length L of the ring. The formula used to calculate the refractive index of the ring is given below:

$$n_{\text{eff}} = \left(\frac{L_{\text{coupling}}}{L}\right) n_{\text{eff,coupling}} + \left(\frac{L_{\text{bend}}}{L}\right) n_{\text{eff,bend}} + \left(\frac{L_{\text{straight}}}{L}\right) n_{\text{eff,straight}} \tag{3.4}$$

Using this effective refractive index of the entire ring resonator and the wavelength, a value for the length of the ring resonator can be determined at which it resonates at a specific wavelength.

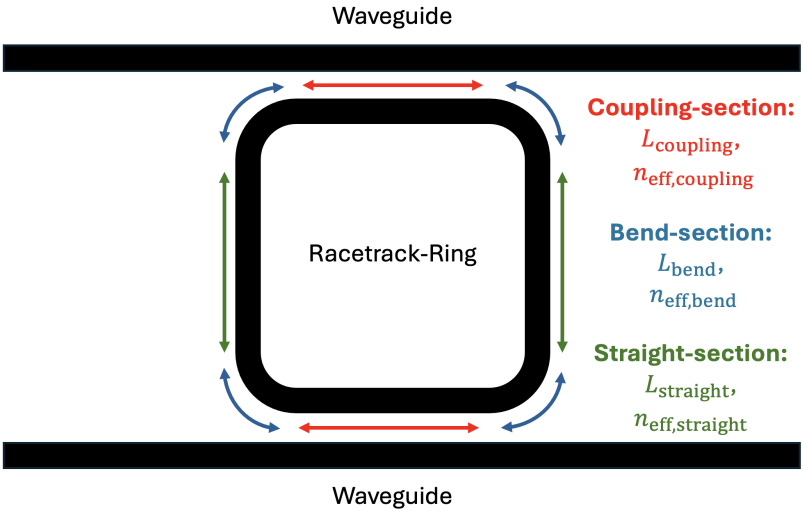

Figure 18: Sections for the calculation of the effective refractive index. The respective lengths L_{i} and the refractive indices $n_{\mathrm{eff,\,i}}$ for the sections are indicated.

3.2.6 Calculations for Bragg Filters

Of particular interest for the Bragg gratings that determine the transmission and reflection of the Bragg filters in this case is the average effective refractive index n_{eff} for the Bragg grating structure, as the periodicity of the grating depends on it, which determines the central wavelength λ_{B}. Since the average width of the Bragg grating corresponds to the width of the straight waveguides used, the refractive index of the straight waveguides was taken as the best initial approximation for the average refractive index for the Bragg gratings. In addition to the central wavelength, the bandwidth with which the light is reflected by the grating is also crucial. This depends on the group index n_{g} and the coupling coefficient κ, which is a measure of reflectivity within the Bragg grating. The parameters needed for the exact calculation of the bandgap were not determined within the scope of this thesis but were carried out by Frank Brückerhoff-Plückelmann who works in the same research group. Using the simulations for the group index, a python program was used by him in which the bandwidth can be entered as a predefined input.
The results for the effective refractive index from the straight section of the ring resonator which are used here as explained can be found in section 6 listed in table 8. Using these effective indices and the formula 2.47, the periodicities of the Bragg gratings for the respective filters were subsequently

determined. The periodicities for the Bragg filters with $\lambda_B = 1550$ nm to $\lambda_B = 1570$ nm in 1 nm intervals were subsequently determined to test how well the theoretical results match the experimental ones. Various values for the bandgap were also tested on the test chip.
In addition to the parameters for the Bragg gratings, the length of the directional coupler, where the light is split 50:50, must also be determined. Since directional couplers are among the most commonly used components in PICs, measurements from the group can also be utilized here.

3.3 Measurement Techniques

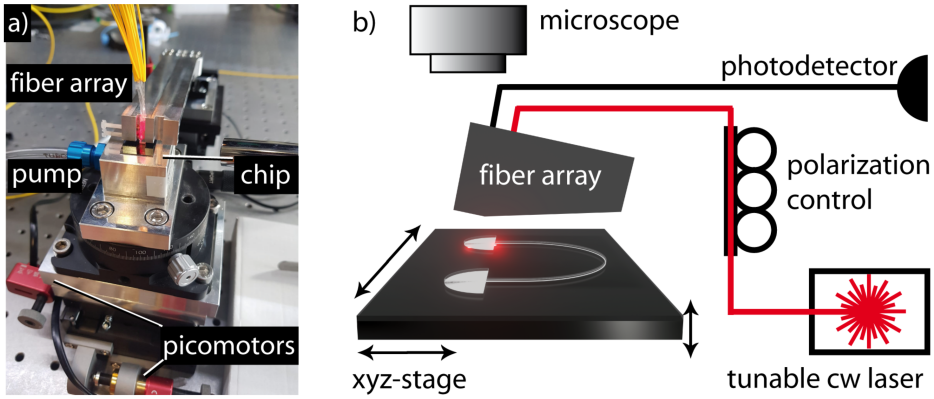

Figure 19: a) Measurement setup used with the chip, the fiber array and control mechanisms. b) Schematic representation of the measurement process, figure taken form [18] p. 20.

The principle according to which the measurements for the bachelor's thesis were recorded is described in the following. In figure 19, the stage on which the chip to be examined is placed is shown. The chip is then fixed, a with vacuum pump to ensure it does not move during the measurement. Above the table is the fiber holder, which holds the optical fibers and at its end is the fiber array. The crucial property of the fiber array is that the channels are spaced at a fixed distance of $d = 127\,\mu$m. The accuracy in the spacing of the channels in the fiber array is important, as all input and output grating couplers [19] being measured are arranged vertically parallel to each other with this same precise spacing. The grating couplers are components used to couple light from free space into waveguides and vice versa. They thus serve as the input and output ports for the light to the individual structures being measured [9]. Additionally, the fiber array is positioned at an angle of 8° to the vertical axis which causes the light to propagate through the air

at an angle of 11° this ensures, that the transmission into and out of the grating couplers is maximized. By moving the chip using the stage, the fiber array can be aligned with the grating couplers of the specific structure to be measured within micrometer precision. A tunable laser covering the wavelength range of interest is then connected to one channel of the fiber array, and photodiodes[1] are connected to the outputs of the fiber array that need to be measured. Using a program that can control the laser's wavelength and synchronize the recorded data from the photodiodes, it is possible to perform a wavelength sweep and observe how the structure behaves depending on the wavelength. The data recorded by the photodiodes are saved as csv files and can be analyzed subsequently. An example of an individual structure to be measured, in the form of a ring resonator, is shown in the following figure.

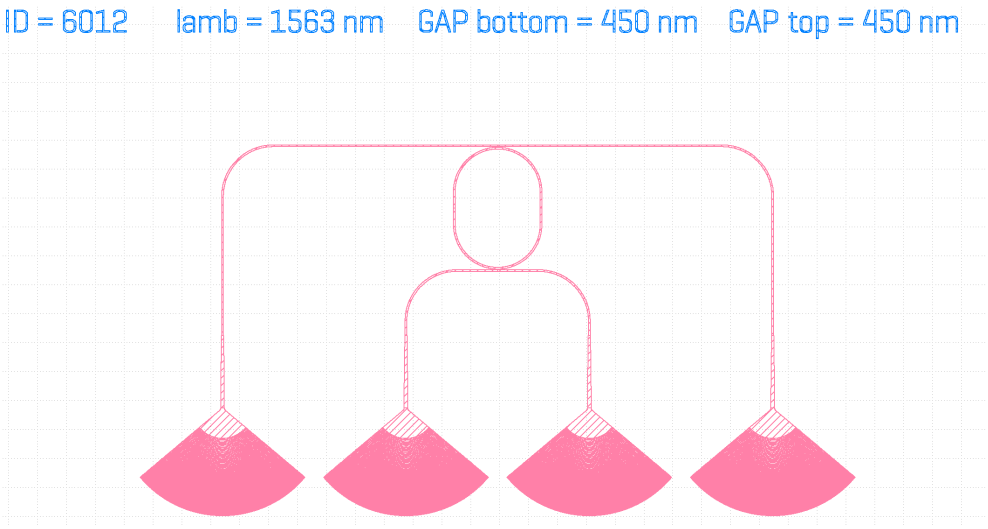

Figure 20: Image of a ring resonator. At the bottom of the image, the four grating couplers are visible, through which light is coupled in and out. The ring resonator to be measured is connected to these grating couplers via waveguides.

[1]Optical Receiver, 900-1700 nm InGaAs Detector, 200 kHz Bandwidth, M4

4 Results

In the course of this thesis, two photonic chips were designed and subsequently fabricated. In figures 21 and 22 are schematic illustrations of the fabricated chips. The respective sections are numerated and will be considered and explained subsequently. Parameter sweeps for ring resonators and

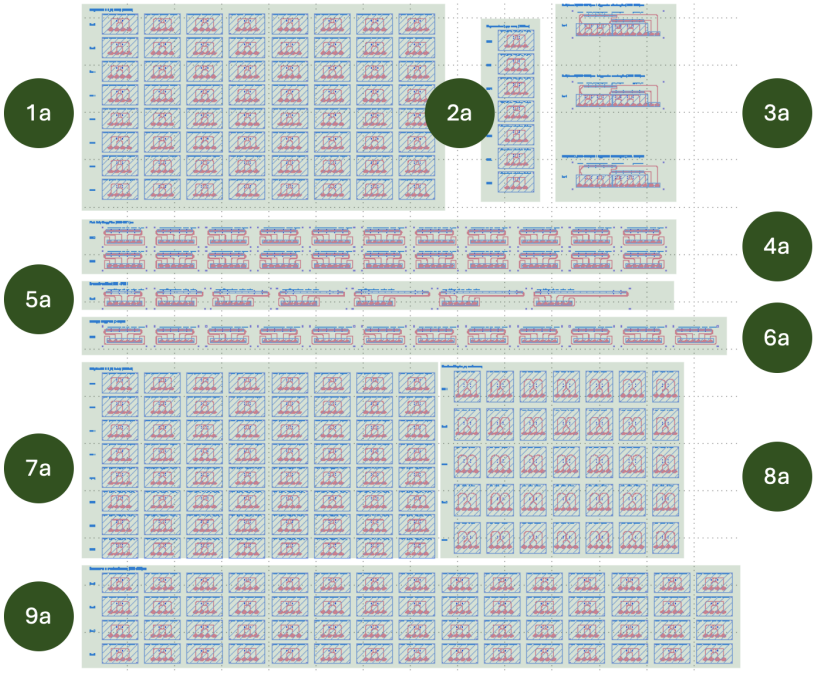

Figure 21: Illustration of the first chip, on which parameter sweeps were conducted for ring resonators, Bragg filters, and directional couplers across various sections, along with the construction of test multiplexer structures. The different sections are labeled, and these labels are subsequently referenced.

Bragg filters were performed on both chips to later investigate how the theoretical results differ from the experimental ones. Additionally, the fabrication of two chips allowed for an estimation of the reproducibility of the results. The fabricated chips were taken from the same wafer to minimize variations between the chips. The structures on the first chip were examined after fabrication, and the insights gained from these measurements were used to design and meassure a second chip, on which the building block parameters were altered based on the experimental findings. In addition, identical structures were built on the chips to test reproducibility for very delicate components.

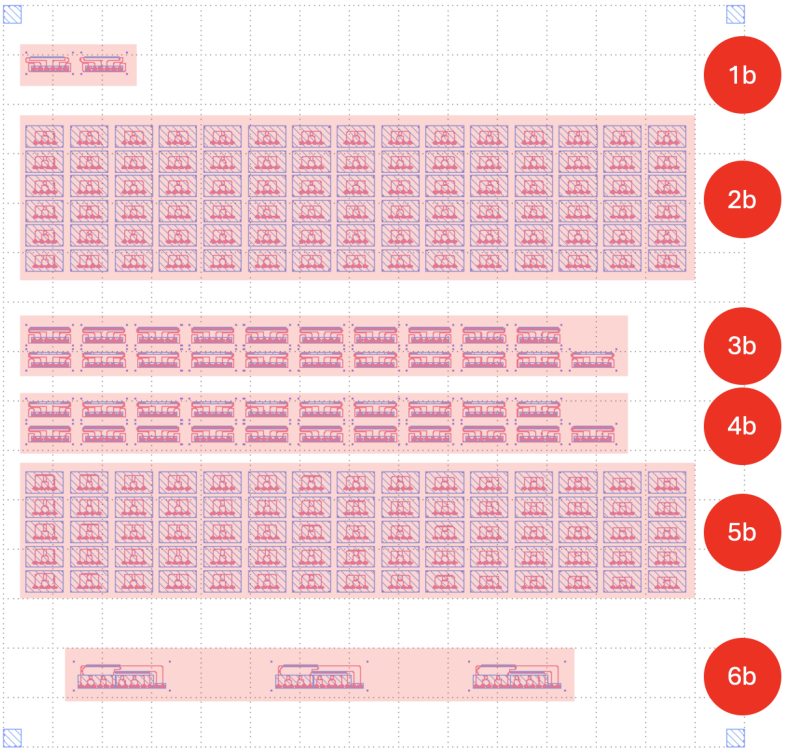

Figure 22: Illustration of the second chip, containing sections where parameter sweeps were performed for ring resonators and Bragg filters. The sections are labeled, and these labels are subsequently referenced.

4.1 Ring Resonators

4.1.1 Free Spectral Range

As described in section 3.2.3, the group index n_g was simulated for the FSR. The complete results for these simulated values can be found in table 7. The simulated values ranged from $n_g = 2.09732$ for $\lambda = 1550$ nm to $n_g = 2.12123$ for $\lambda = 1570$ nm. Subsequently, the maximum lengths of the ring resonators were calculated to ensure an FSR of 4 nm. Thus, the maximum length of the ring resonators is in the range of approximately $L = 286\,\mu$m for $\lambda = 1550\,$nm to $L = 290\,\mu$m for $\lambda = 1570\,$nm.
For the comparison of the theoretical FSR with the one measured on the chip, section **2b** is considered first. This section contains symmetric ring resonators where the length L of the ring was swept in the vertical straight section without changing the coupling region and the bends. Additionally both gaps of the ring resonators were swept. The relevant parameters of the

ring resonators in the section under consideration are given in the table 1. The minimum and maximum FSR are calculated using formula 2.42 with the simulated group indices.

Table 1: Varied parameters of section **2b**.

gap range [nm]	L range [μm]	$\mathrm{FSR}_{\mathrm{theo}}$ range [nm]
200 - 450	232.5 - 235.5	4.886 - 4.995

The measurements are conducted as described in section 3.3. Light is incoupled into the input port, and the spectra of the drop and through ports are measured. The recorded CSV files are then analyzed in Python, where a Lorentzian function is fitted to the resonance peaks of the ring resonators, and its center is determined. In figure 23, a typical recorded spectrum is shown. The difference between each pair of consecutive peaks is then calcu-

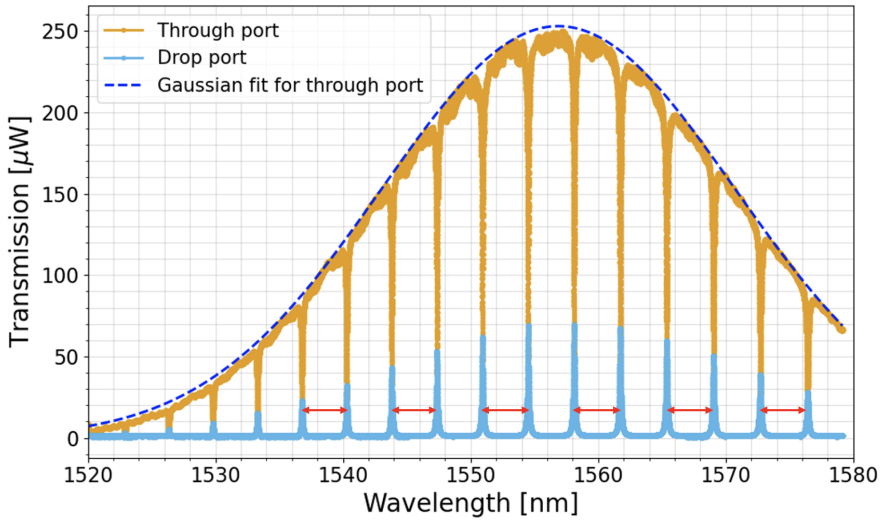

Figure 23: Measured spectrum of the through and drop ports of a ring resonator, with a plotted envelope for the through port spectrum. The Gaussian shape of the spectrum, characteristic of the transmission of the grating couplet, is clearly visible. Additionally, the FSR is marked in red between the transmission peaks. The Lorentzian shape of the peaks in the drop port spectrum is also recognizable.

lated, and the average of these differences is determined. Finally, the standard deviation of this mean value is computed. The wavelength dependency of the FSR is not taken into account because, in the considered wavelength

range, no such dependency is observed in combination with the accuracy of the fitting function. The experimentally determined value, including errors is provided below.

$$\mathrm{FSR}_{\mathrm{exp}} = (5.13 \pm 0.12)\,\mathrm{nm} \tag{4.1}$$

This results in a deviation of 1.13σ to 2.03σ between the theoretically calculated values and the experimentally measured ones. The absolute deviations between the theoretical values in table 1 and the experimentally determined value are ranging from 4.2% to 2.7%. The deviations can be attributed, on the one hand, to the manufacturing of the wafer, which does not have a perfectly smooth surface but can vary in height within the nanometer range compared to the manufacturer's specifications. On the other hand, the deviations are due to the fabrication of the photonic circuits on the wafer.

4.1.2 Coupling Length and Gap

To find the optimal parameters for coupling, we first theoretically investigate how different coupling parameters affect the transmission behavior of the ring resonator at the drop port. In the following we are considering a symmetric ring resonator with identical coupling regions at the input and waveguides, the coupling constants κ are also equal in both regions. The loss is denoted by α. For the following considerations, figure 24 depicting the behavior of an ideal ring resonator at a resonance frequency is used as the basis.
The simulation shown in figure 24 represents the ideal case for light at a resonant wavelength. The figure shows the intensity of the E-field. The source is placed at the input port in the upper waveguide on the left with an intensity of $I_{\mathrm{i1}} = 1$, and we monitor the drop port in the lower waveguide, also on the left. Additionally, it is interesting to note that the field in the ring resonator is significantly increased due to the in section 2.3 explained constructive interference of the light with itself. It is also evident that the intensity on the right side of the waveguide is higher than on the left side, as light couples into the lower waveguide, causing the intensity there to be lower than on the right half of the ring.
To determine the optimal parameters, it is first useful to examine how the quantities of interest vary with the transmission coefficient t used in 2.40. To do this, we will examine how the maximum transmission at the drop port T_{max}, the extinction ratio (ER), and the finesse (F) behave for a ring resonator with symmetric coupling regions, given fixed values of the loss coefficient α. First, an estimation of the loss coefficient α is provided. The losses for silicon nitride are approximately 2 dB/m [5]. Given a ring length of 280 μm, the

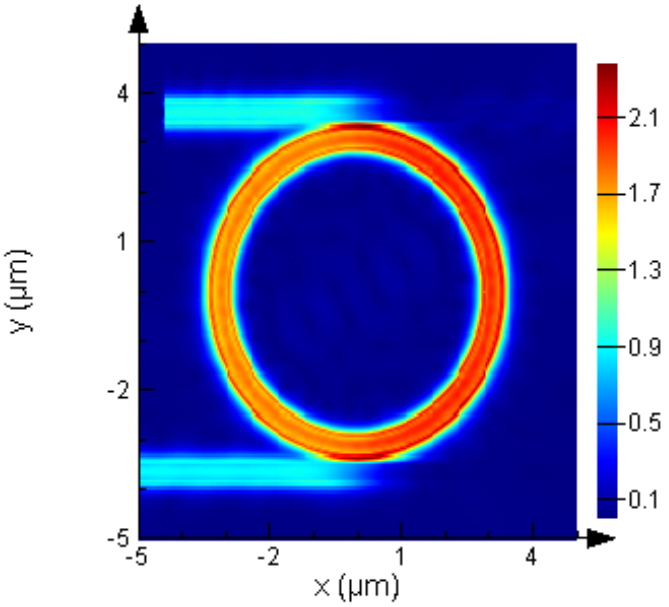

Figure 24: $\vec{E}$-field intensity near a drop resonance, figure taken from [20].

value of α is calculated as follows:

$$\alpha = 10^{\frac{-280 \cdot 10^{-6}\,\mathrm{m} \cdot 2\,\frac{\mathrm{dB}}{\mathrm{m}}}{10}} = 0.999871 \approx 0.9999 \tag{4.2}$$

For the calculated value of α, the variables of interest are now plotted for resonant wavelengths.
Figure 25 shows that the maximum transmission $T_{\max}(t)$ [10] at the drop port occurs at small values of t,

$$T_{\max}(t) = \frac{(1-t^2)^2\alpha}{(1-t^2\alpha)^2} \tag{4.3}$$

corresponding to large coupling coefficients κ. However, it also demonstrates that with very low losses considered ($\alpha \approx 1$), the transmission remains very close to the maximum even for larger transmission coefficients t, and only drops significantly at very high values of t. Intuitively, small values of t indicate that all light is coupled into the ring and then directly coupled out. Higher values of t indicate that a smaller fraction of the resonant light is coupled into the ring, undergoing more round trips inside the ring before being coupled out.
In figures 26 and 27, it is evident that the ER and the finesse increase with

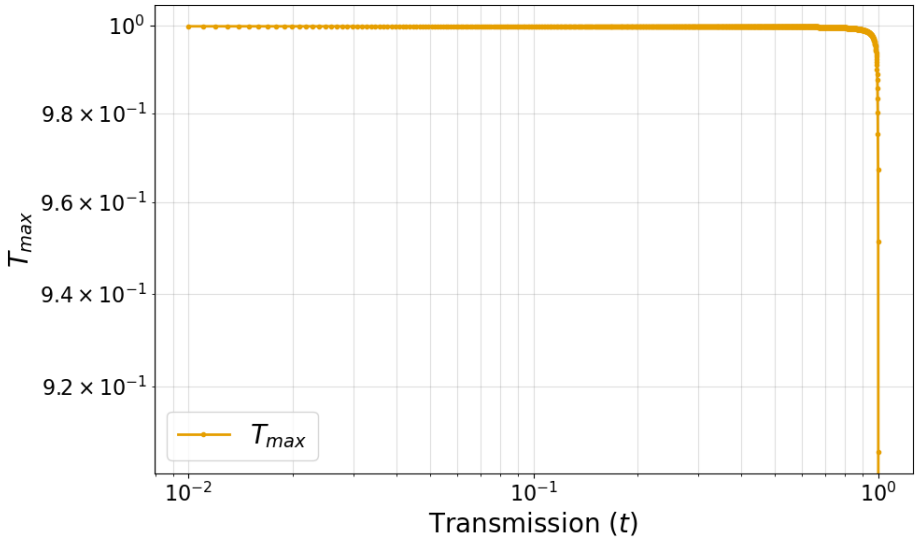

Figure 25: Maximum transmission $T_{\max}$ at the drop port normalized to an input of $I_{i1} = 1$, as a function of the transmission coefficient t for a symmetric ring resonator.

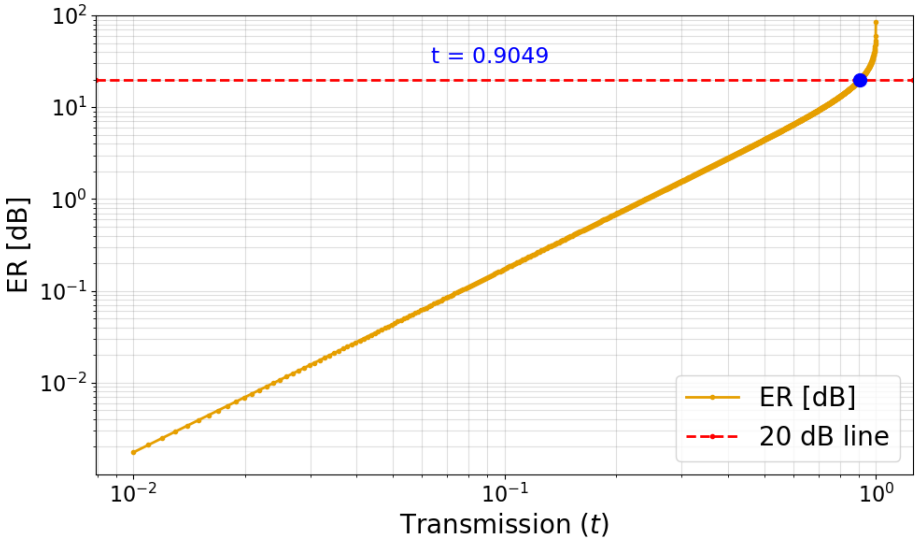

Figure 26: Extinction ratio at the drop port between the minimum and the maximum transmission as a function of the transmission coefficient t for a symmetric ring resonator. Additionally, the 20 dB line is shown, along with the corresponding t value.

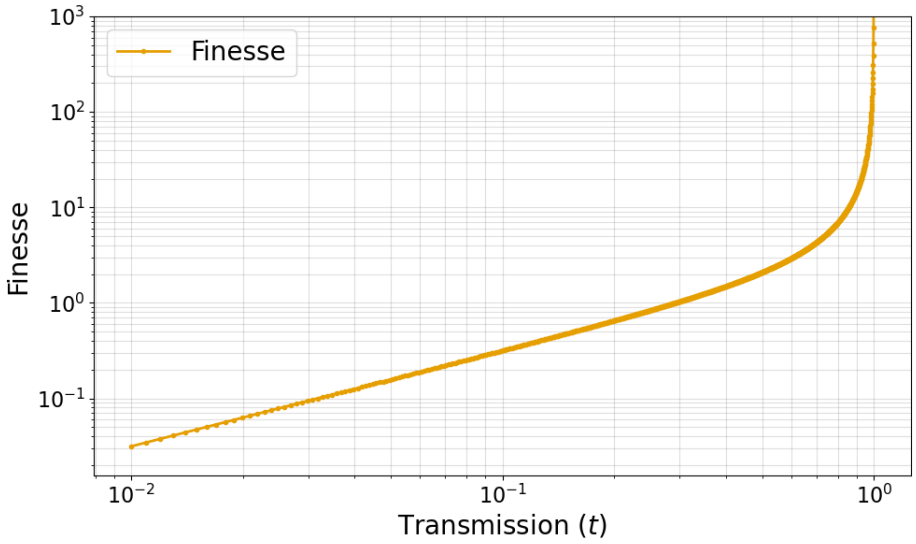

Figure 27: Finesse as a function of the transmission coefficient t for a symmetric ring resonator.

larger values of t. For the ring resonators of the multiplexer, achieving both high transmission and a descent high ER and finesse requires finding an optimum balance between these parameters. Due to the low theoretical losses of the silicon nitride platform used for the PIC, the transmission remains very close to its maximum even at relatively high values of t.
By aiming for an ER of 20 dB, we can now calculate the corresponding transmission coefficient t and from this, determine the coupling coefficient κ as well as the corresponding coupling length. In figure 26 showing the ER, we have the ratio of the maximum transmission to the minimum transmission at the drop port. An ER of 20 dB corresponds to a ratio of 100 between the maximum and minimum transmission. For ER = 100, $t \approx 0.905$, allowing us to calculate the coupling coefficient, which is crucial for determining the coupling length. Using this information about the desired power fraction to be coupled from one waveguide to the other to achieve an ER of 20 dB, the effective refractive indices of the even and odd modes were determined for a fixed gap of 300 nm between the waveguides. Subsequently, using the formula 2.35, the length of the directional coupler was calculated to get an

estimate of how long the coupling region should be.

$$\kappa^2 = 1 - t^2 = 0.095 \tag{4.4}$$

$$L_c = \frac{\arcsin\left(\sqrt{0.095}\right) 1.550\,\mu\text{m}}{\pi(1.559576 - 1.548026)} = 13.38\,\mu\text{m} \tag{4.5}$$

To investigate the influence of the coupling length on the behavior of the ring resonator experimentally, the coupling lengths of the ring resonators were swept in section **5b** while keeping the length of the rings constant. Here symmetrical rings were fabricated, with the coupling length being varied. The measurements in this section have two goals, the first one is determining the coupling length at which an ER of 20 dB is reached, the second one is investigating the transmission and the ER at the drop port as a function of the coupling length. The varied parameters to this section are given in table 2.

Table 2: Varied parameters of section **5b**.

gap range [nm]	L_c [μm]
100 - 300	1, 2, 3, 5, 10, 15, 20, 30, 35, 40, 45, 50, 55, 60, 65

The coupling lengths specified in the table cover a very large range. They were chosen to achieve the two mentioned goals. First, rings with coupling lengths were fabricated in the range where an ER of 20 dB is theoretically expected. Thus, rings with coupling lengths of $L_c = 10, 15, 20\,\mu$m were built, since these are within the range of the value calculated for the coupling length in equation 4.5. Second, rings with short coupling lengths starting at $L_c = 1\,\mu$m which exhibit a coupling constant close to zero, and those with $L_c = 65\,\mu$m, where almost one hundred percent of the light is coupled onto the ring resonaor, were fabricated, using equation 4.5 for the calculation of the coupling constants. For rings with a small coupling length the ER should be maximal and the transmission low according to the theory and for rings with a large coupling length it should be the other way around. In addition to varying the coupling lengths of the rings, the size of the gaps was also adjusted. The focus is on determining how small the gaps can be made while ensuring the results remain reproducible. Investigating small gaps is valuable, as they enable shorter coupling lengths, resulting in more compact ring resonators. This allows for a larger FSR, which is often desirable.
The measurements in this section were also conducted as described in section 3.3, where the wavelengths were swept over the range from 1520 nm to 1580 nm. Similarly to the determination of the FSR, spectra were also recorded

at both the through and drop ports. However, in this measurement, not only the position of the resonance peaks, as in the determination of the FSR, is relevant, but also the ratio of the transmission at the through and drop ports. To obtain comparable results in the absolute transmission at the drop and through ports, two transmission spectra were recorded for the photodiodes used. For this purpose, two grating couplers on the chip were used, which are directly connected by a waveguide. The output signal at the second grating coupler was first recorded with one photodiode, and then the second photodiode was connected to this output to record the spectrum with it under otherwise unchanged settings. This allows the normalization of one spectrum to the other which was necessary, as they record spectra of different intensities even under the same settings. Furthermore, it should be noted that the connections between fibers also represent a calibratable uncertainty. Through the calibrations it was ensured that the transmission levels of the spectra are comparable. For the measurements of the ring resonators, it was found that with very small gaps, specifically those smaller than 200 nm, meaningful measurement results are often not observed, since the spectra do not exhibit characteristics of ring resonator spectra but only show noise. This is attributed to frequent fabrication inaccuracies in such small structures. Therefore, the rings with a 300 nm gap, as calculated in the theoretical section, are considered. First, the rings with a coupling length of $L_c = 10, 15, 20\,\mu$m are examined. To ensure the accurate representation of the data, since the grating couplers do not transmit all wavelengths equally well but rather around an optimal wavelength in a Gaussian distribution, as seen in figure 23, the plots had to be also normalized to this effect.
The plots for the ring resonators with the mentioned coupling lengths are shown in figures 28 to 30. The ER shown in the plot is the experimentally determined maximum ER between the minimum and maximum transmission in the range from 1550 nm to 1570 nm for the drop port. The plots align well with the expectations described in section 3.2.4.
There, in equation 4.5 it was calculated that an ER of 20 dB is achieved at a coupling length of approximately $13.38\,\mu$m for a gap of 300 nm. In figure 28, it is seen that the ER of 20 dB is reached at a coupling length of $10\,\mu$m. The fact that the experimentally determined coupling length is shorter than the theoretical one can be explained by the calculation not considering the region where the ring's curves approach the waveguide near the coupling length. This effect artificially extends the length of the coupling region. Therefore, it becomes evident that it is crucial to perform parameter sweeps on a test chip to assess how significantly this effect influences the results. The conducted sweeps have thus led to the conclusion that the desired ER of 20 dB is achieved at a coupling length of $10\,\mu$m, and that the trans-

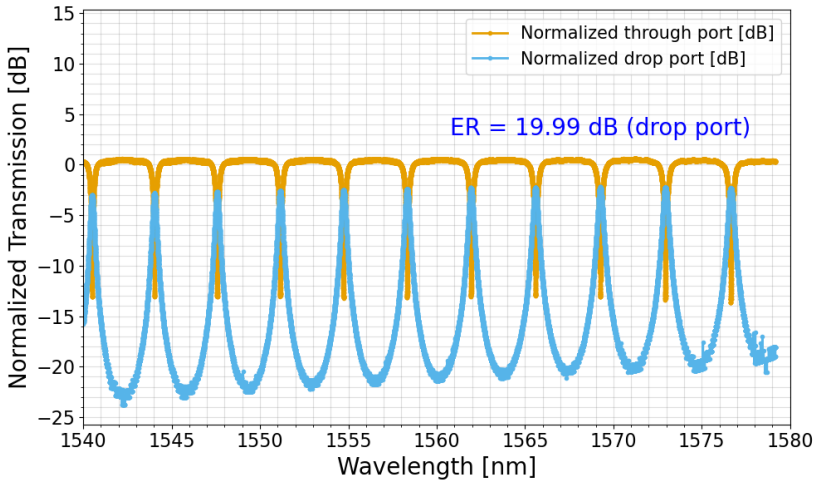

Figure 28: Spectra at the drop and through ports normalized to the envelope of the transmission curve at the through port. For a ring resonator with a gap of 300 nm and $L_c = 10\,\mu$m. The transmission is $T \approx 53\%$.

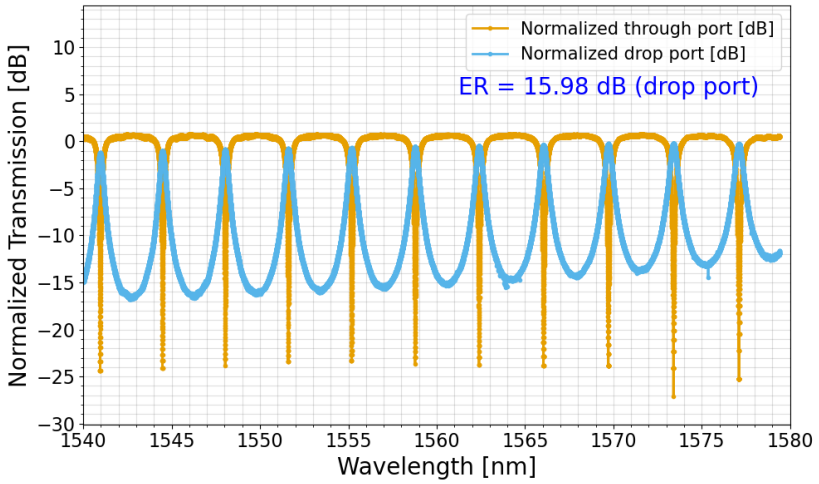

Figure 29: Spectra at the drop and through ports normalized to the envelope of the transmission curve at the through port. For a ring resonator with a gap of 300 nm and $L_c = 15\,\mu$m. The transmission is $T \approx 75\%$.

mission, from the envelope of the drop port to the envelope of the through port, reaches approximately $T \approx 53\%$.

The second goal is to examine how the ER behaves as a function of the

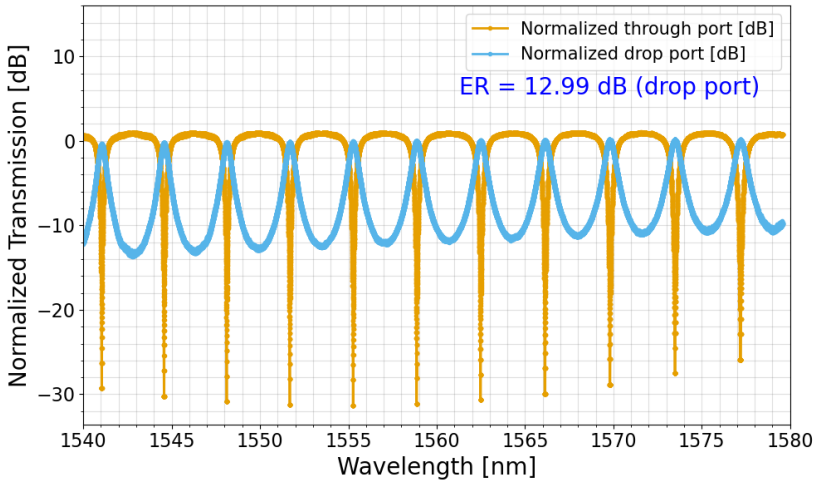

Figure 30: Spectra at the drop and through ports normalized to the envelope of the transmission curve at the through port. For a ring resonator with a gap of 300 nm and $L_c = 20\,\mu$m. The transmission is $T \approx 85\%$.

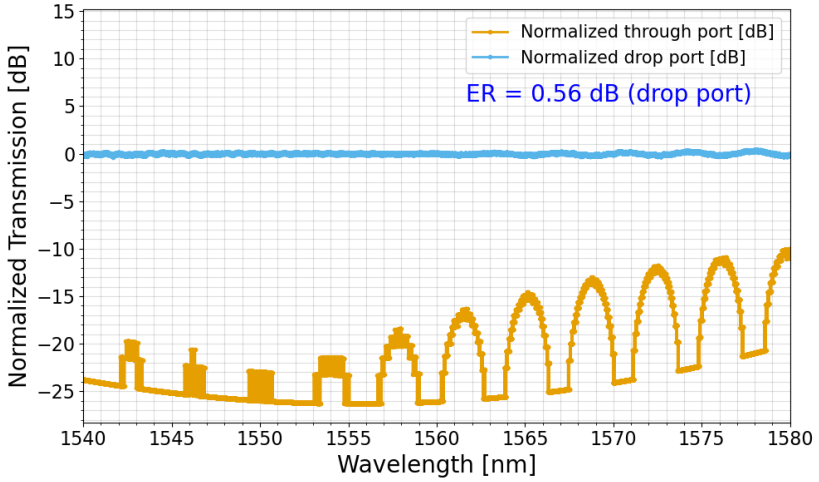

Figure 31: Spectra at the drop and through ports normalized to the envelope of the transmission curve at the through port. For a ring resonator with a gap of 300 nm and $L_c = 60\,\mu$m. The transmission is $T \approx 100\%$.

transmission. Unlike the previous section, the focus here is not on finding a specific ER, but rather on observing the general behavior. For this purpose, figure 32 illustrates the relationship between the ER and the transmission.

The measurements reflect the general relationship between the ER and the

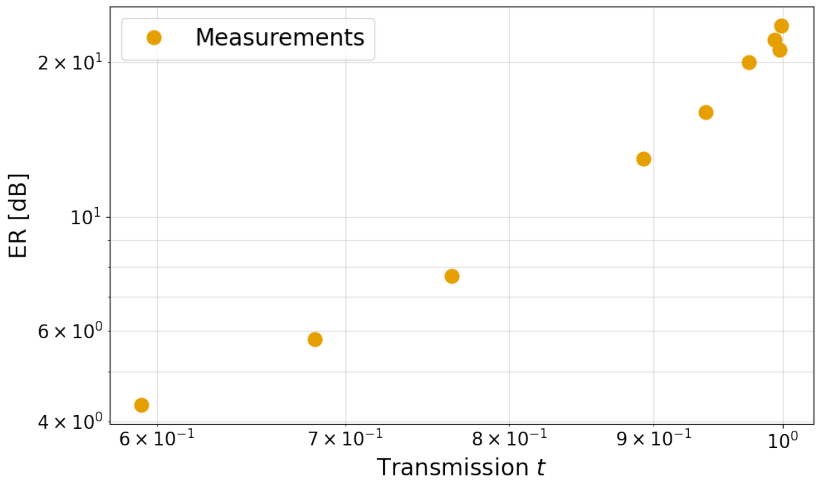

Figure 32: Shown are the experimental values for the ER as a function of the theoretical value for the transmission t for the respective coupling length.

transmission, as predicted by theory and shown in figure 26. Both plots are presented in a double logarithmic scale, and the measurements reveal a qualitatively similar trend. With increasing transmission, the ER also increases significantly.
In addition, figures 28 to 31 can be used for this purpose. Firstly, the prediction that the ER decreases with increasing coupling length, thus with greater coupling, is confirmed. Secondly, it is also evident that the transmission T increases with increasing coupling length. In the extreme case, at almost the maximum coupling length of 60 μm, it is observed that the light couples to the ring resonator independently of wavelength. This occurs because all the light is coupled into the ring in the lower coupling region of the ring resonator and immediately coupled out again at the top. As a result, the characteristics of the ring namely constructive and destructive interference are lost. This is clearly illustrated in Figure 31. Here, the transmission is independent of wavelength, and the ER is minimal. Additionally, the finesse decreases with increasing coupling length until it approaches zero at a coupling length of 60 μm. At this point, the wavelength dependence of the transmission, as mentioned, is eliminated.
In figures 33 and 34, the finesse and the ratio of the envelope of the drop port to envelope of the through port T are shown. In the figure 33, a qualitatively similar trend to the theoretical curve is observed, as shown in figure 27. Thus, it also holds that the finesse increases with greater transmission t. For

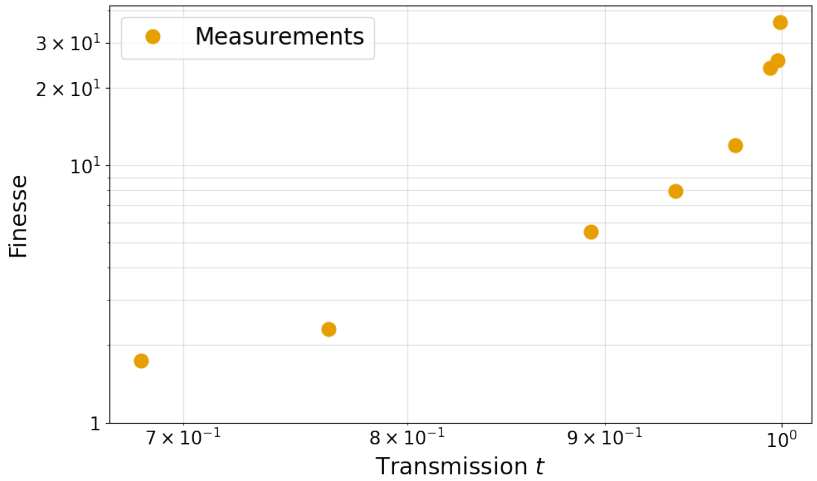

Figure 33: Illustration of the experimental results for the finesse as a function of the theoretical value for the transmission t for the respective coupling length.

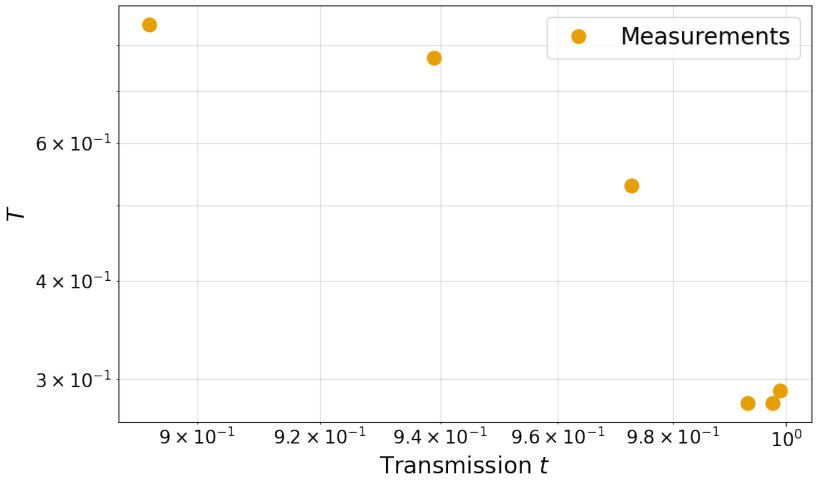

Figure 34: Illustration of T, the ratio of the envelope of the drop port to envelope of the through port, as a function of the theoretical value for the transmission t for the respective coupling length.

the ratio of the envelope of the drop port to envelope of the through port T, it is evident that for larger values of t, this ratio decreases. The three closely spaced points in the lower right of figure 34, at high values of t, are unexpected and likely due to fitting errors. In comparison with figures 25 to 27, it can qualitatively be confirmed that a higher T requires accepting a

lower finesse and ER, and vice versa.

4.1.3 Resonance Wavelength

In the following section, we will examine the resonance wavelengths of the ring resonators. The measurements have two main objectives: first, to investigate how the experimentally determined resonance wavelengths λ_{res} respectively the effective refractive indices $n_{\text{eff}}(\lambda)$ of the ring resonators differ from the theoretical values, and second, to assess the reproducibility of the results. Ring resonators are extremely sensitive, and high accuracy in the resonance wavelength is required for the multiplexer. Through these measurements, it is possible to accurately determine the resonance wavelength of the ring resonators, allowing for subsequent adjustments using methods such as silicon implantation and temperature tuning to achieve the desired wavelength. For the construction of the multiplexer, it is essential that the resonance wavelength of each ring resonator is tuned to within one nanometer of the desired wavelength. Otherwise, it will not be possible to correct this with heat tuning and silicion implantation. These requirements place very high demands on the fabrication of the ring resonators. To achieve the two aforementioned goals, two rows of ring resonators with identical parameters were constructed on each of the two chips. This allowed us to measure the deviation of the resonance wavelengths and the effective refractive indices of the ring resonators from the theoretical values twice, as well as to assess the reproducibility of identical structures. The two mentioned rows are located in sections **9a** and **2b** on the respective chips. In these sections, the length of the symmetric ring resonators was varied in the horizontal direction, and the gaps were varied in the vertical direction.
The measurements were also conducted as described in section 3.3, where the spectra were recorded at both the drop and through ports. To determine the resonance frequencies, Lorentzian curves were fitted to the resonance peaks in the spectrum of the drop port, similar to the procedure used for determining the FSR. The center of each fit represents the identified resonance peaks. As before the wavelengths were swept over the range from 1520 nm to 1580 nm.
The relevant parameters as well as the theoretical and the measured resonance wavelengths for the ring resonators in the two rows that were compared are listed in table 3. The number of ring resonators in a given row in sections **9a** and **2b** differs from the number indicated in table 3 because the recorded data for two of the ring resonators proved to be invalid upon analysis. The values given in the table for the theoretical wavelengths for each ring length were calculated using the effective refractive index for the entire ring derived

in section 3.2.5 and equation 2.37 for $m = 233$. This value for m was chosen because, at this value, the theoretical resonance wavelengths are closest to the measured resonance wavelengths being considered. The value is therefore the best estimate for the theoretically predicted resonance wavelength.

Table 3: Varied parameters and measurement results for the two rows in sections **9a** and **2b**.

gaps [nm]	Length [μm]	λ_{theo} [nm]	λ_{exp} [nm] (**2b**)	λ_{exp} [nm] (**9a**)
300	232.65	1550.78	1549.13	1548.69
300	232.80	1551.53	1550.11	1549.61
300	232.95	1552.29	1550.88	1550.23
300	233.10	1553.04	1551.75	1551.03
300	233.40	1554.55	1553.12	1552.67
300	233.55	1555.31	1553.87	1553.58
300	233.70	1556.06	1554.55	1553.35
300	234.00	1557.57	1556.24	1555.25
300	234.15	1558.32	1557.00	1555.97
300	234.30	1559.07	1557.55	1556.62
300	234.45	1559.82	1558.46	1557.33
300	234.60	1560.58	1558.92	1558.81
300	234.75	1561.33	1559.18	1558.90

The values in table 3 are illustrated more clearly in figure 35, which also includes fitted lines and error bands. The error for the values from section **9a** is 0.18 nm, while for those from section **2b** it is 0.15 nm. This results in average σ-deviation for the measurement series in section **9a** is about $\Delta_{9a} = 12.1\sigma$, while the average σ-deviation for the measurement series in section **2b** is $\Delta_{2b} = 10.0\sigma$.
It is evident from this that the simulated effective refractive indices, on which the theoretically determined values for the resonance wavelengths are based, exhibit a significant deviation from the actual values. Consequently, these cannot be used to accurately predict the resonance wavelength of the ring resonators after fabrication. Additionally, it has been observed that there are significant deviations between the two series, particularly because they do not fall within their respective error margins. Since the resonance wavelength of the ring resonators can only be increased through the two methods of heat tuning and silicon implantation, the minimum of the experimentally determined effective refractive index, which is proportional to the resonance wavelength, is used here. Table 9 in section 6 shows the experimentally determined minimum refractive indices, assuming a linear relationship between

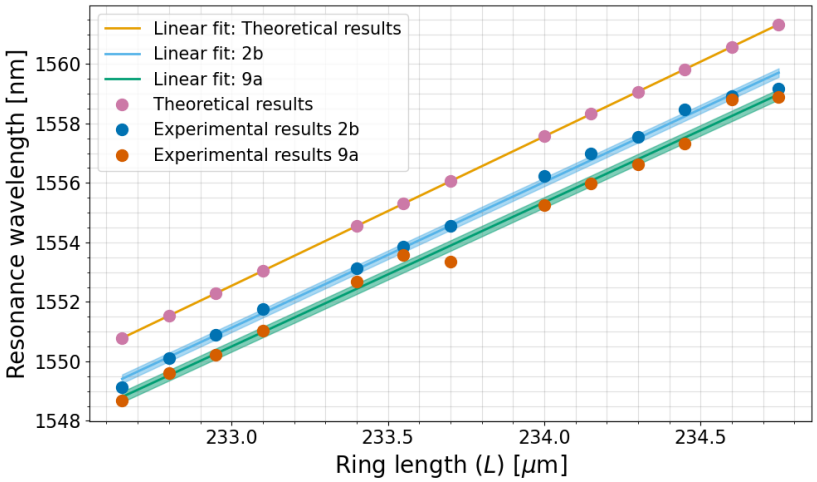

Figure 35: Theoretical and experimental results for the resonance wavelengths λ_{res} corresponding to the respective ring lengths L, as well as linear fits and error bands for the experimental results. The width of the error bands corresponds to the standard deviation between the trend line and the values.

the resonant wavelengths or the refractive index and the ring length.

4.2 Bragg Filters

4.2.1 Bandwidth

When determining the bandwidth, there are two main goals. First, we observe the deviation between the theoretical and the experimental values across a range to determine the deviation in relation to the size of the bandwidth. Second, assess the reproducibility of the bandwidth, by examining Bragg filters with the same designed bandwidth across two chips. The necessary simulations to determine the group index n_g are not conducted as part of this bachelor's thesis, as previously mentioned. Instead, existing simulations from the research group for the platform Si_3N_4 used in the multiplexer are utilized. Here, measurements were conducted as described in section 3.3, where the spectra at the drop and through ports of the Bragg filter were recorded. The recorded data is then plotted, and the reflected spectrum at the drop port was fitted with an FWHM. The bandgap in equation 2.48 differs from the experimentally determined one in that it considers the distance between the first minima adjacent to the central wavelength. However, the FWHM is more relevant for the multiplexer parameters, as we are design-

ing multiple Bragg filters to cover the entire wavelength spectrum. Figures 36 and 37 show the recorded spectra of the Bragg filters for two different bandwidths.

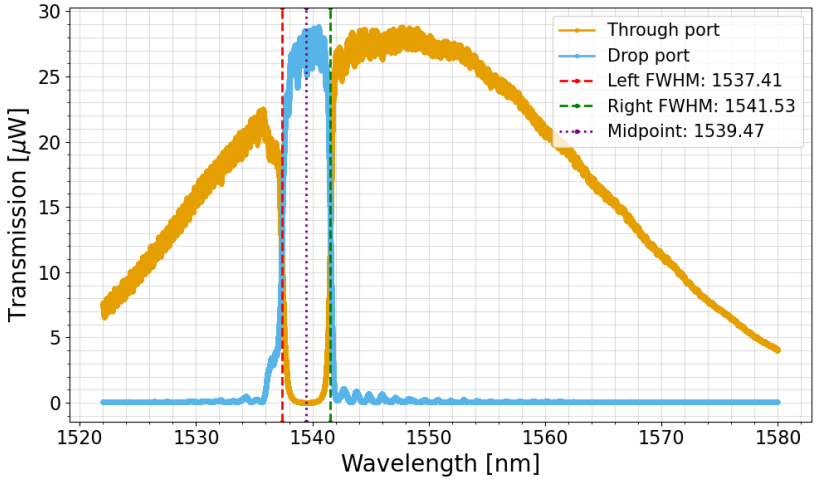

Figure 36: Measured spectra of the through and drop ports of a Bragg filter with a theoretical bandwidth of 3 nm and a periodicity of 500 nm. The experimentally determined bandwidth is 4.12 nm.

To observe the changes in bandwidth, section **6a** was considered, where the bandwidth was swept over a larger range to evaluate potential deviations of the bandwidth more comprehensively. The relevant parameters and results for section **6a** are presented in table 4.

Table 4: Varied parameters and results of section **6a**.

$\text{bandwidth}_{\text{theo}}$ [nm]	$\text{bandwidth}_{\text{exp}}$[nm]	deviation [nm]
2	3.35	1.35
3	4.12	1.12
4	4.89	0.89
6	6.67	0.67
7	7.99	0.99
8	8.53	0.53
9	9.31	0.31
10	10.05	0.05
11	10.80	-0.20

An average deviation of approximately 0.6 nm can be observed. It is notable

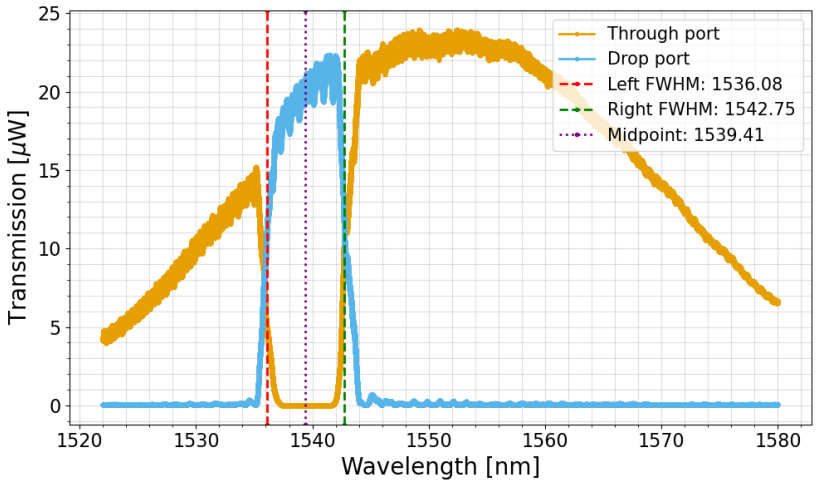

Figure 37: Measured spectra of the through and drop ports of a Bragg filter with a theoretical bandwidth of 6 nm and a periodicity of 500 nm. The experimentally determined bandwidth is 6.67 nm.

that the deviations between the theoretical and experimental values decrease towards larger bandwidths, reaching a minimum at 10 nm. In the range of 4 nm to 5 nm bandwidth, there is a deviation of about one nanometer between theory and experiment.
To determine the reproducibility of a specific bandwidth, sections **4a** and **4b** are examined. In these sections, the periodicity of the Bragg gratings is varied, resulting in different center wavelengths λ_B. The filters in both sections all have a theoretical bandwidth of 5 nm. Thus, reproducibility can be investigated in two aspects: first, how the bandwidth behaves with changes in the Bragg wavelength λ_B on a single chip, and second, the deviations between chips with the same bandwidth and a simular wavelength. The same measurement and evaluation methods as those used in the previous section are applied here, although the midpoint between the two FWHMs is additionally provided as the best estimate for the Bragg wavelength. Table 5 lists the parameters and results for the bandwidth for those filters where the Bragg wavelengths of the filters are approximately equal. The averages and standard deviations of the bandwidths listed in table 5 demonstrate that the results within a measurement series are well reproducible, as the standard deviations are each less than 0.1 nm. Furthermore, it is evident that the deviations between the two chips are also very small, with an absolute deviation of less than 0.1 nm and a sigma deviation of $\Delta = 0.65\sigma$.

Table 5: Comparison of the bandwidths of the Bragg filters from sections **4a** and **4b** with theoretical bandwidths of 5 nm with similar wavelengths.

bandwidth, λ_B [nm] (**4a**)	bandwidth, λ_B [nm] (**4b**)
6.30, 1551.1	6.26, 1550.8
6.25, 1552.4	6.31, 1552.0
6.23, 1553.7	6.30, 1553.5
6.17, 1554.4	6.11, 1555.1
6.34, 1555.6	6.41, 1555.5
6.16, 1556.7	6.32, 1556.9
6.19, 1557.8	6.38, 1557.7
6.25, 1558.1	6.36, 1558.3
6.30, 1559.8	6.37, 1559.4
$\varnothing = (6.24 \pm 0.06)$ nm	$\varnothing = (6.31 \pm 0.09)$ nm

4.2.2 Center Wavelength

The second important property of the Bragg filters that we want to consider is the Bragg wavelength. To determine this, equation 2.47 is used. The periodicity corresponding to the wavelength λ_B must be entered into the program from which the Bragg gratings are created. To calculate the average effective refractive index of the Bragg gratings, as mentioned in section 3.2.6, the effective refractive index of a waveguide made of the same material with the same average width is used. From the average effective refractive index corresponding to the respective wavelength and the wavelength, the periodicity is then determined. On the first chip, parameter sweeps are conducted in section **4a**, where filters with a simulated wavelength ranging from 1550 nm to 1570 nm are built.

Subsequently, the sections are measured, and the central wavelength is determined again by fitting two FWHMs and determining the center. There are significant deviations between the theoretically expected Bragg wavelengths and the actually measured ones. For the measured section **4a**, an average deviation of 10.5 nm is determined.

Thus, the simulated average effective refractive indices do not match the real ones very well. To determine the real effective refractive indices, the refractive index is calculated from the measured wavelengths and the corresponding periodicity. Assuming a linear behavior of the refractive index in the range from 1540 to 1570, the refractive indices for the larger wavelengths were calculated. On the second fabricated chip, parameter sweeps for the Bragg filters are performed again in section **3b**, using the experimentally

determined effective refractive indices from the first chip to determine the periodicities. Table 6 presents a comparison between the theoretical values and the experimental values.

Table 6: Comparison of theoretical and experimental Bragg wavelengths with periodicities for sections **4a** and **3b**.

λ_{theo} [nm]	λ_{exp}, Λ [nm] (**4a**)	λ_{exp}, Λ [nm] (**3b**)
1551	1539.94, 500.54	1550.82, 505.12
1552	1541.24, 500.97	1551.97, 505.55
1553	1542.69, 501.41	1553.48, 505.98
1554	1543.94, 501.85	1555.07, 506.42
1555	1544.50, 502.28	1555.53, 506.85
1556	1545.81, 502.72	1556.94, 507.29
1557	1546.61, 503.16	1557.72, 507.72
1558	1547.49, 503.61	1558.32, 508.15
1559	1548.54, 504.05	1559.42, 508.59
1560	1549.35, 504.49	1559.91, 509.02
1561	- , 504.94	-, 509.46
1562	1551.05, 505.38	1562.00, 509.89
1563	1552.41, 505.83	1563.03, 510.33
1564	1553.67, 506.27	1564.52, 510.76
1565	1554.44, 506.61	1564.89, 511.20
1566	1555.57, 507.06	1566.88, 511.63
1567	1556.74, 507.50	1567.93, 512.07
1568	1557.81, 507.95	1568.86, 512.51
1569	1558.09, 508.40	1569.49, 512.94
1570	1559.77, 508.85	1570.52, 513.38
-	$\varnothing = (10.5 \pm 0.3)$ nm	$\varnothing = (0.5 \pm 0.4)$ nm

The average deviation of the measured wavelengths from the theoretically calculated ones is given, as well as the standard deviation of this value. The absolute deviation from the theoretical value on the first chip in section **4a** is more than 20 times greater than that on the second chip in section **3b**. Thus, a significant improvement in accuracy is achieved through the experimental determination of the effective refractive index.

5 Conclusion

5.1 Discussion

The following discussion will address what the experimental results obtained in Chapter 4 imply for the design of the multiplexer.
The measured FSR results of the ring resonators show a good agreement, within 0.24 nm, between the values based on the simulated group index n_g and the experimentally obtained ones, which can be calculated using equation 2.42. Therefore, these values are reliable for FSR calculation.
The evaluation of the experimental results for the coupling length and gap shows that the prediction can be confirmed that, for ring resonators, the importance of individual properties such as ER, transmission, or finesse must be weighed against each other for the specific application. For instance, achieving a very high ER must be balanced with the fact that the transmission in this ring will be lower compared to a ring with very high transmission but very low ER. For the application in the multiplexer, achieving the highest possible transmission is desired. However, an ER of at least 20 dB should also be maintained. This extinction ratio was achieved at a coupling length of $L_c = 10\,\mu$m and a gap of 300 nm. Consequently, we must accept that the transmission in our case is only around $T = 53\%$, which must be compensated for by a higher input power from the laser. Nevertheless, this loss is acceptable because it only occurs once and in parallel for 20 ring resonators, in contrast to a network of cascaded directional couplers where a loss of 50% occurs sequentially at each coupler. Here, the measurements can also be considered successful, as they provide the necessary parameters for the multiplexer.
Concerning the resonance wavelength of the ring resonators we now have a better understanding of the variability and offset in our measurements. Specifically, we assume there is a constant offset relative to the theoretical values, combined with variability due to fabrication differences. This again highlights the sensitivity of the resonance wavelength of the ring resonators. However, the objective of achieving reproducibility of the results within the accuracy required for the fabrication of the ring resonators used in the multiplexer can be considered fulfilled, as the discrepancies between the two measurement series are small enough to allow for future deviations to be managed after fabrication. This will be further explained in section 5.3. For the construction of the multiplexer, since the wavelength of the rings can only be tuned upwards, the effective refractive index of the lower measurement series will be used as a basis. The experimentally determined values for these refractive indices are found in table 9.

For the bandwidth of the Bragg-Filters, as shown by the bandwidth sweeps in table 4, there is a notable discrepancy between the theoretical and experimental bandwidths, particularly at lower bandwidths, with a difference of about one nanometer. However, it is also evident that, as shown in table 5, the bandwidths are reproducible across different chips. The results demonstrate that the current calibration can be used to achieve the desired outcomes.
Regarding the center wavelength of the Bragg-Filters, the average deviation of the center wavelength at (0.5 ± 0.4) nm is still too large to rely solely on it for constructing narrow Bragg filter wavelengths for the multiplexer. For the final determination of the Bragg wavelength, it is necessary to use thermal tuning or silicon implantation after the fabrication of the multiplexer chip to accurately set the wavelength of the Bragg filters. This is because the Bragg filters in the multiplexer should have an accuracy of less than 0.4 nm to function optimally. However, achieving such accuracy is generally challenging because the period of these filters is in the range of 500 nm, and a difference of 1 nm or less represents the difference between two adjacent laser wavelengths.

5.2 Summary

The goal of this thesis has been to develop a WDM system with ring resonators and Bragg filters as its main components. The primary task has been to approximate the necessary parameters for the system through simulations and then precisely determine them through the construction of PICs and their measurement. This multiplexer will be used to build the transmitter side of a QKD system, aiming to achieve a record-high data transfer rate.
Starting from a description of the theoretical physical principles necessary for the work, an initial concrete design proposal for the multiplexer was presented and discussed. The functionality of this multiplexer served as the basis for determining the parameters required. Subsequently, the methods required to determine the parameters were described, along with the tools needed for this purpose. Simulations were used to determine the initial parameters for all necessary quantities, which were then swept across two chips designed during the course of the work. The chips were subsequently measured in order to test the simulated values and also check the reproducibility of the results. The key parameters of particular interest were the resonance wavelength, the FSR, coupling, and ER for the ring resonators. For the Bragg filters, the focus was on investigating the bandwidth and resonance wavelength. The comparison between the simulated parameters and the experimentally obtained results revealed significant deviations within the required accuracy

for constructing the WDM system. However, it was also observed that the results are mostly sufficiently reproducible for practical use.
Overall, it can be concluded that within the scope of this work, the parameters necessary for the multiplexer have been determined mostly with sufficient accuracy.

5.3 Outlook

Following this bachelor thesis, three main tasks need to be addressed. Firstly, once the sender chip with the lasers is completed, it will be essential to precisely characterize the lasers on the chip and determine their exact wavelength ranges, as the lasers on this chip are expected to exhibit slight deviations from the theoretical wavelengths. Secondly, once the transmitter chip has been characterized, the design proposal for the multiplexer chip will need to be fabricated with parameters that match those of the transmitter chip. Finally, the individual components of the multiplexer chip, namely the ring resonators and the Bragg filters, will need to be tuned. In particular, tuning the chip through silicon implantation and temperature tuning will play a significant role. Similar to the approach taken in the bachelor thesis, simulations for temperature tuning will be required, followed by experimental verification of these simulations. For silicon implantation, existing knowledge from the research group can be leveraged.

6 Appendix

6.1 Simulations for Estimating the Group Index

Table 7: Simulation results for the group index.

λ_{res} [μm]	n_{g}
1.55000	2.09732
1.55104	2.09851
1.55208	2.09970
1.55312	2.10089
1.55417	2.10210
1.55521	2.10330
1.55626	2.10451
1.55731	2.10622
1.55836	2.10744
1.55941	2.10867
1.56046	2.10990
1.56152	2.11114
1.56257	2.11239
1.56363	2.11363
1.56469	2.11489
1.56575	2.11615
1.56681	2.11741
1.56787	2.11868
1.56893	2.11995
1.57000	2.12123

6.2 Simulations for Estimating the Effective Index

Table 8: Simulation results for the effective index.

λ_{res} [μm]	n_{eff}
1.55000	1.54969
1.55100	1.54934
1.55200	1.54899
1.55301	1.54864
1.55401	1.54829
1.55501	1.54794
1.55602	1.54759
1.55703	1.54724
1.55804	1.54688
1.55905	1.54653
1.56006	1.54617
1.56108	1.54582
1.56209	1.54546
1.56311	1.54510
1.56412	1.54475
1.56489	1.54448
1.56591	1.54412
1.56693	1.54377
1.56795	1.54341
1.56897	1.54305
1.57000	1.54269

6.3 Experimental Results for Refractive Indices and Ring Lengths

Table 9: Experimental results of the minimum of the refractive indices and ring lengths.

λ_{res} [μm]	L [μm]	n_{eff}
1550.00	232.897	1.55069
1551.00	233.103	1.55031
1552.00	233.310	1.54994
1553.00	233.516	1.54957
1554.00	233.722	1.54920
1555.00	233.929	1.54883
1556.00	234.135	1.54846
1557.00	234.342	1.54809
1558.00	234.548	1.54772
1559.00	234.754	1.54735
1560.00	234.961	1.54698
1561.00	235.167	1.54662
1562.00	235.374	1.54625
1563.00	235.580	1.54588
1564.00	235.786	1.54552
1565.00	235.993	1.54515
1566.00	236.199	1.54479
1567.00	236.405	1.54443
1568.00	236.612	1.54407
1569.00	236.818	1.54370
1570.00	237.025	1.54334

References

[1] Shor, P. W., *Polynomial-Time Algorithms for Prime Factorization and Discrete Logarithms on a Quantum Computer* SIAM Journal on Computing. 26 (5), 1484–1509 (1997)

[2] Bernstein, D.J., *Introduction to post-quantum cryptography. In: Bernstein, D.J., Buchmann, J., Dahmen, E. (eds) Post-Quantum Cryptography* Springer, Berlin, Heidelberg (2009)

[3] Tomamichel, M., Leverrier, A., *A largely self-contained and complete security proof for quantum key distribution.* Quantum 1, 14 (2017)

[4] Beutel F. et al., *Fully integrated four-channel wavelength-division multiplexed QKD receiver* Optica 9, 1121-1130 (2022)

[5] imec, *Silicon nitride photonics platforms with extremely low propagation loss.* `https://www.imec-int.com/sites/default/files/2023-01/Silicon%20nitride%20photonics%20platforms.pdf` [online] accessed 2024/07/07.

[6] Osgood jr. R. , Meng X., *Principles of Photonic Integrated Circuit*, Springer, Berlin, Heidelberg (2021), p. 31-36, p. 317-323

[7] Liu J. M., *Photonic Devices*. Cambridge University Press , Cambridge (2005), p. 73-79, p. 206-209

[8] Saleh, B. E. A., and Teich, M. C., *Fundamentals of Photonics*. John Wiley & Sons, Ltd, Chichester(2007), p. 315-321

[9] Chrostowski L., Hochberg M., *Silicon Photonics Design: from devices to systems*, Cambridge University Press, Cambridge (2015) p. 28-36, p. 117-121, p. 163

[10] Bogaerts W. et al., *Silicon microring resonators*. Laser Photonics Rev. 6, No. 1, 47–73 (2012) p. 51

[11] Rabus D. G., Sada C., *Integrated Ring Resonators Chapter 2*. Springer Nature Switzerland AG (2020), p. 3-13

[12] Simard A., LaRochelle S., *Complex apodized Bragg grating filters without circulators in silicon-on-insulator*. Opt. Express 23, p. 16662-16675 (2015)

[13] Varri a. et al., *Scalable Non-Volatile Tuning of Photonic Computational Memories by Automated Silicon Ion Implantation.* Advanced Materials, vol 36, issue 8 (2023)

[14] Gehring H., Eich A., Pernice W.H.P., *Broadband out-of-plane coupling at visible wavelengths.* Opt. Lett. 44, 5089-5092 (2019)

[15] Ansys Lumerical guide *MODE - Finite Difference Eigenmode (FDE) solver introduction.* `https://optics.ansys.com/hc/en-us/articles/360034917233\protect\penalty\z@-MODE-Finite-Difference-Eigenmode-FDE-solver-introduction` [online] accessed 2024/06/26

[16] Yee K. S., *Numerical solution of initial boundary value problems involving Maxwell's equations in isotropic media.* IEEE Transactions on Antennas and Propagation. 14, (1966) p. 302–307

[17] K. Luke et al. *Broadband mid-infrared frequency comb generation in a Si3N4 microresonator.* Opt. Lett. 40, 4823-4826 (2015)

[18] Spreter V., *Realization of Broadband Si3N4 Directional Couplers using Partial Euler Bends.* Bachelor thesis (2023)

[19] D. Taillaert et al. *Grating Couplers for Coupling between Optical Fibers and Nanophotonic Waveguides.* Japanese Journal of Applied Physics, vol. 45, no. 8a, pp. 6071-6077, (2006)

[20] Ansys Lumerical guide *Ring resonator getting started - Design and initial simulation.* `https://optics.ansys.com/hc/en-us/articles/360042800293-Ring-resonator-getting-started-Design-and\protect\penalty\z@-initial-simulation` [online] accessed 2024/07/03

[21] QPIT Münster Revision *Docs Welcome to the gdshelpers' documentation!.* `https://gdshelpers.readthedocs.io/en/latest/` [online] accessed 2024/06/27

[22] Gillies S. et al., *Shapely 2.0.4 documentation* . `https://shapely.readthedocs.io/en/stable/#` [online] accessed 2024/06/27

[23] Lifante G., *Integrated Photonics: Fundamentals*, John Wiley & Sons, Ltd, Chichester(2003), p. 61-63

List of Figures

List of Tables

Acknowledgments

My thanks first go to Prof. Dr. Wolfram Pernice, who made it very easy for me to start my bachelor's thesis in his research group.
I would also like to extend my special thanks to Julius Römer, who, as my direct supervisor, always had an open ear for my questions and answered them in a very calm and friendly manner. Additionally, he assisted me with practical matters, whether in the lab or with technical issues.
Furthermore, I would like to thank Philipp Lohmann and Jan Brandes, who, alongside Julius, were always available for questions and provided practical help with programming.
I also want to thank Liam McRae for his assistance with problems related to Lumerical, as well as for the use of the automated measurement setup, which significantly saved time.
Additionally, I would like to thank Prof. Dr. Lauriane Chomaz for agreeing to serve as the second examiner for my thesis.
I also extend my thanks to the entire research group, as it provided a very cheerful and pleasant working atmosphere in which I had the privilege of writing my thesis.
I would also like to thank my mom for proofreading this thesis and providing me with valuable feedback.
Finally, my deepest gratitude goes to Ingmar Kloß, who has supported me with his wise advice and extensive knowledge since the first day of my studies, and without whom I would not have reached the point of writing my bachelor's thesis.

Erklärung

Ich versichere, dass ich diese Arbeit selbstständig verfasst und keine anderen als die angegebenen Quellen und Hilfsmittel benutzt habe.
Heidelberg, den 22.08.2024,

Linus Alexander Kürpick